Research Report 2015–06

Assessment of predicting and simulating the tropical Pacific climate with APCC Coupled General Circulation Models

Seon Tae Kim

APCC
APEC CLIMATE CENTER

Research Report 2015-06

Assessment of predicting and simulating the tropical Pacific climate with APCC Coupled General Circulation Models

Seon Tae Kim

APCC
APEC CLIMATE CENTER

PREFACE

There have been increased requests for accurate seasonal forecasts due to the socioeconomic and environmental impacts of severe climatic phenomena. It has also been demonstrated that the fully Coupled General Circulation Model (CGCM) is the ultimate tool for sub-seasonal to seasonal climate prediction. Recognizing this, the Asia-Pacific Economic Cooperation (APEC) Climate Center (APCC) has made great efforts to develop and improve a CGCM to provide more reliable forecast information for the Asia-Pacific region.

For the operational use of a CGCM model, we need to evaluate the ability of the model to simulate and predict observed climate features in order to calibrate the seasonal forecast. Along with other possible methods to produce more accurate seasonal forecasts, better initial conditions could help to improve seasonal forecasting skills. It is well known that the tropical Pacific is key in understanding and predicting global climate variations. In particular, El Niño-Southern Oscillation (ENSO) that resides in the tropical Pacific has significant statistical links with global seasonal climate anomalies. Therefore, a principal test of a global coupled climate model will test if it is able to produce reliable simulations of the climate in the tropical Pacific.

This project mainly focuses on improving seasonal forecast skill regarding the climate in the tropical Pacific through applying improved ocean-atmosphere initialization schemes, and also on analyzing model's ability to simulate the observed tropical Pacific climate.

From this study, we may obtain background information on the APCC CGCM's

systematic errors when simulating the observed topical Pacific climate, and also we may increase a level of the forecast skills of the ENSO mode. Since ENSO is capable of having great impacts on weather and climate world wide, these improvements would contribute to better seasonal forecasts by the APCC multi-model ensemble forecast system.

We would like to express deep gratitude to Ms. Hye-In Jeong from APCC's Climate Analysis Team for performing a number of hindcast simulations and providing scientific comments. The success and achievement of this study would not have been possible without her support. We also would like to thank to Profs. Myung-In Lee and Joong-Bae Ahn for their insightful comments and suggestions.

Dr. **Chin-Seung Chung**, Director
APEC Climate Center
January 2016

ABSTRACT

This project examines the systematic biases of the APEC Climate Center (APCC) coupled models (i.e., CCSM3 and SCoPS) in simulating the observed tropical Pacific Ocean climate and the El Niño-Southern Oscillation (ENSO). It is found that the APCC coupled models can capture the key observed features of the tropical Pacific climate and the ENSO. Particularly, some advantages are found in the SCoPS model that will replace the CCSM3 model for operationally forecasting seasonal climate. For instance, the SCoPS model can more realistically simulate the observed asymmetric features of the annual mean rainfall in the meridional direction, and the annual cycle of the sea surface temperature (SST) and zonal winds along the equator. The temporal evolution patterns of equatorial SST anomalies, the zonal wind anomalies, and the anomalous zonal currents associated with the ENSO are better simulated by the SCoPS model. However, both models have several biases with respect to the observations. These include a cold bias in the central equatorial Pacific and a warm bias in the extratropical northeastern and southeastern Pacific Ocean, a thermocline that is too diffuse, precipitation that is too strong in off-equatorial regions, an ENSO shifted to the west which extends too far westward, and the underestimation of the zonal advective feedback, thermocline feedback and thermodynamic damping among the ENSO related feedbacks. This project also attempts to improve the initial conditions in the CCSM3 model for better ENSO forecasts. With the GODAS nudging initialization method, where initial conditions are generated in a coupled simulation performed with the simulated ocean temperatures nudged to those of the reanalysis, the CCSM3 model has better ability

in predicting the ENSO amplitude, global SSTs, and extratropical air temperatures. This is possibly due to the reduced initialization shock, which is a severe problem in predictions using the GODAS method, where the ocean reanalysis data is used as the initial conditions without a nudging process. To improve further the forecasting skill for strong ENSO events or ENSO amplitude, we also implement the GODAS-WIND nudging method, where not only 3-D ocean temperatures but also surface winds are nudged to their observations. However, there is no discernable improvement of the ENSO forecast with the GODAS-WIND nudging initialization method except for forecasts initialized in the late spring. It is also found that the APCC CCSM3 model has a year-to-year variation in the forecasts for the tropical Pacific and the global SST, which is due strongly to changes in the ENSO intensity. That is, a level of their forecast skill increases with the ENSO intensity. Since this result implies the importance of obtaining accurate ENSO amplitude forecasts in order to obtain the better global and tropical Pacific SST predictions, we also attempt to find possible reasons for the increasing errors of the ENSO amplitude in the APCC CCSM3 model with increases in forecasting lead times using the BJ index analysis. Based on a series of analysis including the BJ index, we conclude that the forecasting error for the ENSO amplitude may be related to the tropical Pacific cold bias, which strongly affects the intensity of the thermocline feedback.

CONTENTS

1. INTRODUCTION

There have been increased requests for accurate seasonal forecast due to the socioeconomic and environmental impacts of severe climatic phenomena. It has also been demonstrated that the fully Coupled General Circulation Model (CGCM) is the ultimate tool for seasonal climate prediction. For more accurate seasonal forecast, we need a CGCM that has high fidelity in simulating observed atmospheric and oceanic climate features and it is well known that better initial conditions can help a CGCM to reduce forecasting errors (e.g., Ji et al., 1998; Jin et al., 2008; Hudson et al., 2010).

In a seasonal forecast, the influence of the initial conditions in an atmosphere and ocean model on limiting the predictability has been highlighted, and many methods have been proposed to improve the initial conditions (Chen et al., 1997; Rosati et al., 1997; Ji et al., 1998; Behringer et al., 1998; Kleenlyside et al., 2005; Hudson et al., 2010). Particularly, the importance of ocean initialization has been realized in the seasonal forecast, since the ocean has a long term memory and can influence sea surface temperature (SST) predictions (Jin and Kinter, 2008; Xue et al., 2010; Sun and Ahn, 2015; Kim and Ahn, 2015). The skillful predictions of the SSTs may contribute to better predictions of the global and local climate, since the SSTs can control their associated atmospheric circulations. The methods for the ocean initialization have ranged from simple ones, including the coupled SST nudging method (e.g., Luo et al., 2005; Kleenlyside et al., 2005; Kumar et al., 2014), to the complicated ones, such as the 3- or 4-D variational data assimilation method (Lorenc and Rawlins, 2005). Among them, the SST coupled nudging method, where both atmosphere and ocean initial conditions are produced by running a coupled model with simulated SSTs nudged strongly to the observed ones, can provide a good prediction of the SST variability in the tropical Pacific Ocean (Luo et al., 2005; Kleenlyside et al., 2005; Kumar et al., 2014).

The basis for the simple initialization method is that over regions where ocean variability is controlled by strong atmosphere-ocean interaction, the simulated SSTs nudged to the observations can force the surface wind stress, leading to subsurface temperatures that resemble the observations. This was evidenced by Kumar et al. (2014) from simulations with the early version of the Climate Forecast System (CFS)

that was used operationally for the seasonal forecast at the National Centers for Environmental Prediction (NCEP) in 2004 (Saha et al., 2006). However, the rationale may not be operated in the extratropical latitudes, where the atmospheric internal variability is important and the constraints on wind stress due to SST change have less effect. Therefore, we suggest methods to solve this discrepancy to some extent with a simple initialization method, which is discussed in the following sections.

The benefit of the long-term memory of the ocean is applied to the SST variability associated with the El Niño-Southern Oscillation (ENSO) in the tropical Pacific Ocean, which is the most dominant natural climate fluctuation on interannual time scales (e.g., Rosati et al., 1997). Development of the ENSO involves the Bjerknes feedback (Jin, 1997) between the tropical Pacific trade winds, the SSTs, and the thermocline. During the warm phase of the ENSO, which is referred to as El Niño, the basin-scale warming in the eastern tropical Pacific can cause anomalous westerly winds that in turn induce the flattening of the equatorial zonal thermocline slope and reduce the upwelling of the cold deep water. This leads to enhanced surface warming, which reinforces the wind anomalies. During the cold phase of the ENSO, which is referred to as La Niña, the trade winds and upwelling strengthens and the thermocline slope steepens. The cold anomalies grow further by reinforcing one another. This eastern Pacific anomalous SST change makes the tropical Pacific a key player in understanding and predicting global climate variations. Although the ENSO originates in the tropical Pacific, it has a destructive impact on global climate and weather. This has been evidenced by the significant statistical links between the ENSO and global seasonal climate anomalies such as precipitation and temperature (McPhaden et al., 2006; Philander, 1983; Cai et al., 2014). These links provide an important basis for skillful globe seasonal climate prediction (Latif et al., 1998). Therefore, a principal test of a global coupled climate model is whether it can simulate accurately the tropical Pacific climate and the ENSO.

Although there has been noticeable progress of coupled climate models to simulate the observed tropical Pacific climate and the ENSO, systematic errors in the coupled climate models have been documented in a number of intercomparison studies. The errors include ENSO anomaly patterns that are shifted westward relative to observations, a lack of capturing the observed annual cycle, an inadequacy of

the phase-locking of the ENSO to the annual cycle, a strong Intertropical Convergence Zone (ITCZ) south of the equator in the eastern Pacific, a diffuse equatorial thermocline, a warm bias near the coast of South America, and a cold SST bias in the equatorial central Pacific (e.g., AchutaRao and Sperber, 2002, 2006; Bellenger et al., 2013; Wittenberg et al., 2006; de Szoeke and Xie, 2008; Wang et al., 2014; Kim et al., 2014). These model discrepancies also limit the predictability in the coupled models after the impact of the initial conditions starts disappearing (Goswami and Shukla, 1991; Jin and Kinter, 2009). Furthermore, the importance of the tropical Pacific mean states in simulating the ENSO in coupled models (Battisti and Hirst, 1989; Fedorov and Philander, 2001; Jin et al., 2006; Guilyardi, 2005; Kim et al., 2014) and their interactions have been highlighted in previous studies (Rogers et al., 2004; Sun and Yu, 2009; Choi et al., 2009; Yu and Kim, 2011). Kim et al. (2014) argue that the discrepancy of simulating the ENSO feedbacks in state-of-the-art coupled models (e.g., CMIP models) turns out to be associated with the equatorial Pacific cold tongue bias. Yu and Kim (2011) show that the spatial asymmetries of SST anomalies during El Niño and La Niña phases give rise to a decadal modulation of the ENSO intensity. Hence, a series of bias evaluations on simulating the tropical climate and the ENSO in coupled models may help to identify possible reasons for the ENSO forecast errors.

The APEC Climate Center (APCC) has been operating a CGCM model and making great efforts to provide more reliable forecast information for the Asia-Pacific region. The CGCM is the Community Climate System Model version 3 (CCSM3) (Collins et al., 2006), which was developed in the National Center for Atmospheric Research (NCAR). The APCC CCSM3 model uses the simple oceanic initialization method where 3-D ocean temperature datasets taken from the NCEP Global Ocean Assimilation System (GODAS) (Behringer et al., 1998) are interpolated to the grids used in the ocean model (hereafter referred to as the GODAS method). However, although the GODAS dataset is generated at the NCEP using Geophysical Fluid Dynamics Laboratory (GFDL) Modular Ocean Model (MOM) 3.0 with the 3-D variational data assimilation scheme applied, some problems with the GODAS initialization method such as “initialization shock” and low forecast skill for the ENSO have been identified (Jeong, 2013). Thus, this study will focus on increasing the forecast skill for the ENSO in the APCC CCSM3 model by applying improved (simple) ocean-atmosphere

initialization schemes. Since the model is one of the coupled models of which an APCC multi-model ensemble (MME) prediction system consists, we expect that the seasonal forecast model with demonstrated skill may contribute to the improved seasonal forecasts of the APCC MME prediction system.

We also provide background information on the systematic errors of the APCC CCSM3 model in simulating the observed tropical Pacific climate and on its ability to simulate various properties of the tropical Pacific Ocean climate variability mode, namely the ENSO. In addition, we will also analyze simulations from the APCC new coupled model in order to explore if there is improvement in simulating the tropical Pacific climate. The new coupled model, which is named as the APCC Seamless Coupled Prediction System (SCoPS) coupled model, has been developed with a research team from the Department of Atmospheric Sciencesat the University of Hawaii at Manoa over the last three years and will replace the CCSM3 model for the seasonal forecast.

2. DATA AND METHODOLOGY

2.1 Observational Datasets

We use several observational and reanalysis datasets to validate the simulated climatology and climate variability properties from the APCC coupled models. The simulated SSTs are compared to the SSTs taken from the National Oceanic and Atmospheric Administration Extended Reconstruction of Historical SST (ERSST) (Smith and Reynolds, 2003) data set. The surface wind stresses and the net surface heat fluxes into the ocean are taken from the ECMWF 40-year reanalysis (ERA40) (Uppala et al., 2005). For ocean subsurface quantities, such as the subsurface temperatures, the zonal velocities, and the vertical velocities of the ocean, we use data from the Simple Ocean Data Assimilation Reanalysis (SODA) (Carton and Giese, 2008). The observed precipitation data is taken from the Global Precipitation Climatology Project (GPCP) (Adler et al., 2003) over the period from 1979-2013. Atmospheric variables, other than the wind stress, the net heat flux, and the precipitation, are taken from the NCEP-DOE Reanalysis 2 data set (Kanamitsu et al., 2002).

2.2 Models

For a long coupled simulation analysis, we use a 200-year control simulation from the APCC CCSM3 model, which starts from the last day of a 600 year spin-up simulation of a coupled model from the NCAR. We also analyze a 100-year control coupled simulation from the APCC SCoPS model, which starts from the 500 year spin-up.

The CCSM3 model includes all the component models consisting of the Community Atmosphere Model version 3 (CAM3) (Collins et al., 2004), with a horizontal resolution of T85 (1.4° longitude × 1.4° latitude) and 26 vertical levels; the Community Land Surface Model version 3 (CLM) (Oleson et al., 2004); the Community Sea Ice Model version 5 (CSIM5) (Briegleb et al., 2004); and the Parallel Ocean Program version 1.4.3 (POP) (Smith et al., 1992), with a horizontal resolution of 1° longitude × 1° (1/3° near the equator) latitude and 40 vertical levels.

The SCoPS model consists of atmosphere, land, ocean, and sea ice models. The atmospheric component is the European Centre Hamburg Model (ECHAM, v5.3) with T159 resolution (Roeckner et al., 2003), corresponding to a Gaussian grid of about 0.75° longitude × 0.75° latitude, and 31 hybrid-sigma pressure levels. The land component is an improved bucket model, which is a part of the ECHAM atmospheric model. For the ocean component, we use the POP version 2.0.1, which has a horizontal resolution of 1° longitude × 0.5° latitude and 40 vertical levels. The Los Alamos Sea Ice Model (CICE, v4.1) is used with a resolution of 1° longitude × 0.5° latitude (Hunke and Lipscomb, 2010). The atmosphere-ocean-land-sea ice components of the model are connected with a coupler that is the Ocean-Atmosphere-Sea Ice-Soil (OASIS, v3.0)-Model Coupling Toolkit (Valcke et al., 2012).

2.3 Hindcast Simulations

2.3.1 Initialization Methods

Two initialization methods based on the simple nudging method, which can contribute to the reduction of “initialization shock” (Chen et al., 1997; Luo et al., 2005) that is one of the possible reasons for the low skill in predicting the ENSO with the APCC CCSM3 model using the GODAS method, are applied to the coupled forecast model as follows:

a. ***GODAS nudging method***: We obtain the daily atmospheric and oceanic initialization conditions as restart data from a coupled simulation with simulated ocean temperatures strongly nudged toward the 3-D GODAS ocean temperatures using a restoring time scale of five days. Here, the pentad mean GODAS ocean temperatures are interpolated into daily means using the piecewise linear interpolation method.

b. ***GODAS-WIND nudging method***: In addition to the GODAS nudging method, the simulated surface winds, which are taken from the GODAS datasets, are nudged to observations with a restoring time scale of one hour in order to obtain daily wind initial conditions.

Performance of those initialization methods are investigated using the hindcast simulations of the APCC CCSM3 model, which are carried over the period from 1982-2014 with initialization in all 12 calendar months. For each hindcast year, 5 or 10 ensemble members are generated by using different initial conditions of the atmosphere, land, and sea ice components. That is, for the GODAS and GODAS nudging methods the 10 ensemble members are generated by using initial conditions of the atmosphere, land, and sea ice components on the first, sixth, eleventh, sixteenth, and last five days of each month, while the 5 ensemble predictions with the GODAS-WIND nudging method use the initial conditions in last 5 days of each calendar month. For the oceanic initial conditions, restart data is used from the 24th day of each calendar month, which is the date when the forecasts start.

Predictions at the next month or the next season from the initial condition months are referred to as forecasts at a 0-month lead time. For example, a 0-month prediction for September or for the September-October-November (SON) season starts with initial conditions from August. Similarly, a 1-month (3-month) lead forecast for December or the December-January-February (DJF) season is referred to as a forecast initialized in the month of October (August). Each simulation performs a full seven month integration indicating forecasts from 0-month to 6-month lead times. All analyses are performed based on the ensemble member mean.

The hindcast simulations are verified with the subsurface temperatures and the wind stresses taken from the GODAS reanalysis datasets, since the GODAS datasets are used for the initial conditions. For the verification of the 2-meter air temperature and precipitation, we use the NCEP-DOE Reanalysis 2 data set and GPCP data set, respectively, over the same hindcast period.

2.3.2 Forecast Verification Methods

In this study, we use three general forecast verification methods. We estimate the temporal correlation coefficient (TCC) to measure the strength of a linear relationship between the predicted and the observed variables. In order to evaluate the accuracy of the forecast with respect to the observations, the root mean square error (RMSE) is calculated. For estimating spatial similarity between the forecasts

and the observations, we perform an anomaly pattern correlation coefficient (ACC) analysis.

2.4 Bjerknes Stability (BJ) Index Analysis

We utilize the BJ index formula for quantifying the overall ENSO linear stability (Jin et al., 2006; Kim and Jin, 2011a) and its related air-sea feedbacks in the APCC coupled models and the observations. The BJ index has been found to be a useful tool for a comprehensive and quantitative analysis of the relative contributions of the positive feedbacks and the damping processes to the amplitude of the ENSO variability (Kim and Jin, 2011a, 2011b; Kim et al., 2014; Lübbecke and McPhaden, 2013).

The BJ index is formulated as follows [see Jin et al. (2006) and Kim and Jin (2011a) for a more detailed explanation]:

$$BJ = \frac{R - \varepsilon}{2},$$

where

$$R = -\left(a_1 \frac{\langle \Delta \bar{u} \rangle_E}{L_x} + a_2 \frac{\langle \Delta \bar{v} \rangle_E}{L_y} \right) - \alpha_s + \mu_a \beta_u \left\langle -\frac{\partial \bar{T}}{\partial x} \right\rangle_E + \mu_a \beta_w \left\langle -\frac{\partial \bar{T}}{\partial z} \right\rangle_E + \mu_a \beta_h \left\langle \frac{\bar{w}}{H_1} \right\rangle_E a_h,$$

where BJ is the BJ index, a greater value of which indicates that the tropical climate coupled system supports a stronger ENSO; ε is a damping rate, which is related to the upper ocean adjustment as obtained through a multiple regression using Eqn. (10) of Kim and Jin (2011a); $\bar{u}$, $\bar{v}$, and $\bar{w}$ denote the climatological mean zonal, meridional, and vertical velocities, respectively; $\bar{T}$ represents the climatological mixed-layer (H_1 = 50m) ocean temperatures; $\langle * \rangle$ denotes the boxed area-averaged quantities over the eastern or western region of the equatorial Pacific basin, which are recognized by the subscripts E and W, respectively; L_x and L_y represent the longitudinal and latitudinal length scales, respectively, of the eastern boxed region; and a_1 and a_2 are estimated using the anomalous mixed-layer ocean temperatures averaged zonally or meridionally at the boundaries of a boxed region

and averaged over the box.

The terms of R, which collectively represents the ENSO-related feedback processes of tropical atmosphere-ocean interactions, denotes (from left to right) the mean advection damping (the collective effect of oceanic mean advection and upwelling, which tends to maintain the ocean circulation toward the mean state against variations), the thermodynamic damping (the collective heat flux, in which clouds and evaporation increase in response to warm SST anomalies, the solar radiation, and the latent heat flux into the ocean decrease curtailing the warm anomalies), the zonal advective feedback (the anomalous advection of the mean zonal temperature gradients), the Ekman feedback (the anomalous advection of the mean vertical temperature gradients), and the thermocline feedback (the mean vertical advection of the anomalous vertical temperature gradients).

The thermodynamic damping is estimated with $\langle Q \rangle = -\alpha_s \langle T \rangle_E$ where Q denotes the net anomalous heat flux anomalies into the ocean. The last three positive feedback terms, favoring the SST perturbations that grow, are a product of the mean state and a set of response sensitivity coefficients. Those coefficients are computed from approximated balance equations based on the recharge oscillator theory of Jin (1997), using the least-squares regression method: $[\tau_x] = \mu_a \langle T \rangle_E$, $\langle u \rangle_E = \beta_u [\tau_x] + \beta_{uh} \langle h \rangle_w$, $\langle H(\overline{w}) w \rangle_E = -\beta_w [\tau_x]$, $\langle h \rangle_E - \langle h \rangle_W = \beta_h [\tau_x]$, $\langle H(\overline{w}) T_{sub} \rangle_E = a_h \langle h \rangle_E$.

The balance equations represent, respectively, an anomalous surface wind response (τ_x) to an anomalous mixed-layer ocean temperature (T) change, the response of mixed layer ocean zonal current anomalies (u), the ocean upwelling anomalies (w), and the zonal anomalous equatorial thermocline (h) slope to a wind forcing, and the effect of anomalous thermocline depth changes on ocean subsurface temperature anomalies (T_{sub}). The value of h is estimated as the oceanic heat content anomaly, which is a good proxy for the equatorial thermocline depth change and is defined as the vertically averaged ocean temperatures from the ocean surface to a depth of 300m. The parameter, [τ_x], is the anomalous zonal wind stress area-averaged across the equatorial Pacific (121°E-82°W), and $H(\overline{\omega})$ is a step function to ensure that only the upward vertical motion affects the mixed layer ocean temperature.

Using this analysis, the overall biases in simulating the ENSO feedbacks are estimated, and the errors in predicting the strength of the ENSO events will be associated with the errors in the ENSO feedbacks.

3. LONG COUPLED SIMULATION ANALYSIS

3.1 Annual Mean States

3.1.1 SST

Figure 1 shows the annual mean SSTs from the observations and both coupled models and the difference between the simulated and observed annual mean SSTs in the equatorial Pacific basin. In general, both the CCSM3 and the SCoPS models capture very well the observed zonal asymmetric features (Fig. 1a-c), which are a well-developed equatorial cold tongue in the east side of the basin and a warm pool in the west. However, both models have several biases when compared to the observations. The models both simulate an equatorial cold tongue that is too strong and extends too far to the west relative to the observations, which is linked to the equatorial SST cold bias over the central to eastern equatorial Pacific in the models (Fig. 1d and e).

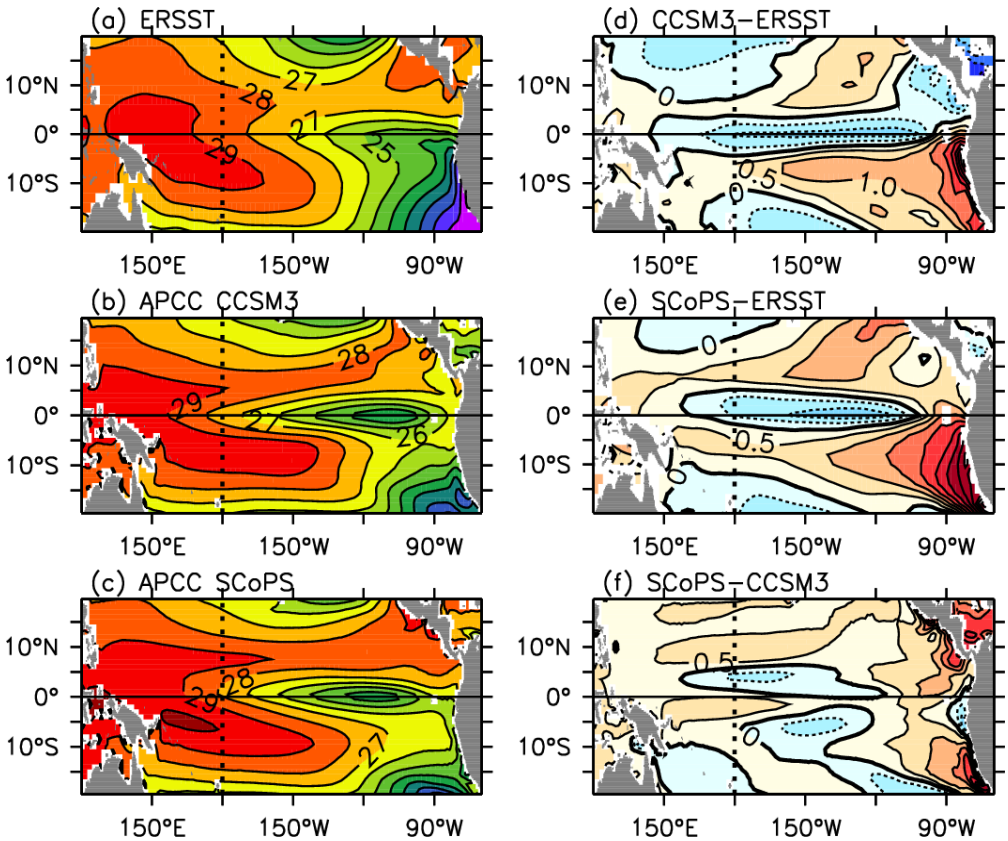

Figure 1 Annual mean SSTs over the tropical Pacific from (a) observations; and (b, c) coupled models (contour interval, C.I., = 1.0 °C); (d, e) model biases of annual mean SST with respect to observations; and (f) difference between the coupled models (C.I. = 0.5 °C). The observations correspond to a time average from the ERSST V2 analysis. The names of the coupled models are indicated.

The cold bias over the cold tongue region reaches to about -1°C in both models. Both models are also characterized by warm biases near South America and those extending from the California coastal regions to near the equator. The warm biases are common discrepancies in other coupled models and have been partly attributed to errors in the simulation of the amount and/or optical thickness of the marine stratocumulus clouds (Yu and Mechoso, 1999; Hu et al., 2011) and to weak meridional winds near the South American coast (de Szoeke and Xie, 2008). The warm biases in the southeastern and northeastern Pacific Oceans and the zonal SST gradient in the western-to-central equatorial Pacific are slightly larger in the SCoPS model than in the CCSM3 model (Fig. 1f).

3.1.2 Surface Winds

Figure 2a-c shows the zonal component of the annual mean equatorial surface wind stress from the coupled simulations and the observations. Overall, it is found that the coupled models simulate the observed characteristics of the mean surface wind stress quite well. Both models have relatively strong easterly winds over the northwestern part of the subtropical regions in the Northern Hemisphere and near the coast of Peru, as shown in the ERA40 observations. Observed weak westerly winds near the eastern boundaries of the equatorial Pacific domain are evident in the model simulations. However, both models do not capture the observed weak westerly winds near the western boundaries of the tropical Pacific Ocean.

As is evident in Figure 2d and e, which display an equatorial surface wind bias with respect to the observations, both models simulate weaker easterly winds than those of the observations in the eastern equatorial Pacific Oceans. Therefore, the cold biases in the eastern equatorial Pacific that are found in both coupled models cannot be attributed to the simulated wind stresses alone; and various processes, such as the complicated interactions with surface wind fields, air-sea heat exchanges, and mixing processes (Cronin et al., 2006), might be involved in the biases. The models simulate stronger equatorial easterly winds to the west of the International Dateline, which is one of possible reasons why the models have a cold tongue extending too far to the west relative to the observations. As displayed in Figure 2f for the difference between climatological wind stresses from both models, the easterly wind biases over the central topical Pacific are larger in the SCoPS model, which seems to be partly due to the stronger zonal SST gradient in the western-to-central equatorial Pacific (see Fig. 1f).

3.1.3 Subsurface Ocean Temperatures

The vertical structure of upper ocean temperatures along the equator from the models and the SODA ocean analysis are shown in Figure 3. We can find some evident biases against the SODA data. Both models have cold biases above the thermocline and warm biases below the thermocline, which indicates that the thermocline is too diffuse in the vertical direction and that the stratification across the thermocline is too weak relative to the SODA reanalysis data. The diffuse thermocline and weaker stratification become worse toward the eastern Pacific Ocean in both models.

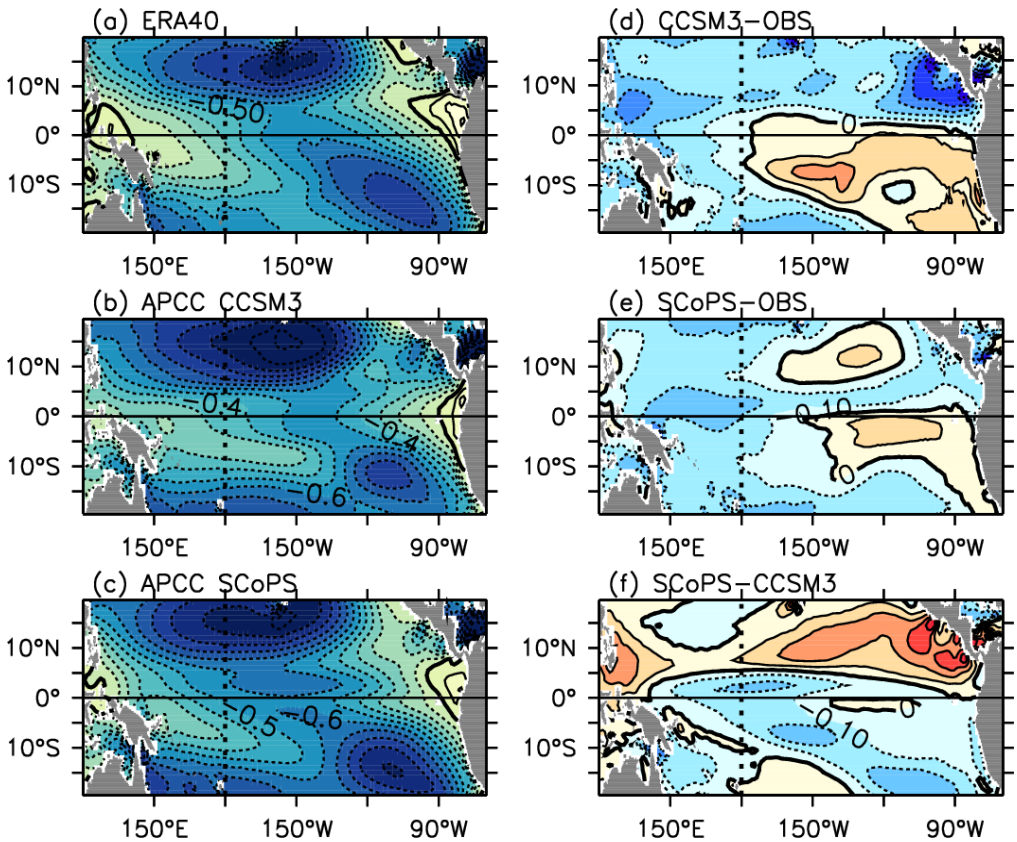

Figure 2 Annual mean tropical Pacific zonal wind stresses (dyne cm^{-2}) from (a) ERA 40 analyses; (b-c) coupled simulations (C.I. = 0.1 dyne cm^{-2}); (d, e) annual mean zonal wind stress biases of coupled simulations with respect to the ERA40 analysis; and (f) difference between the coupled models (C.I. = 0.1 dyne cm^{-2}). The names of the coupled models are indicated.

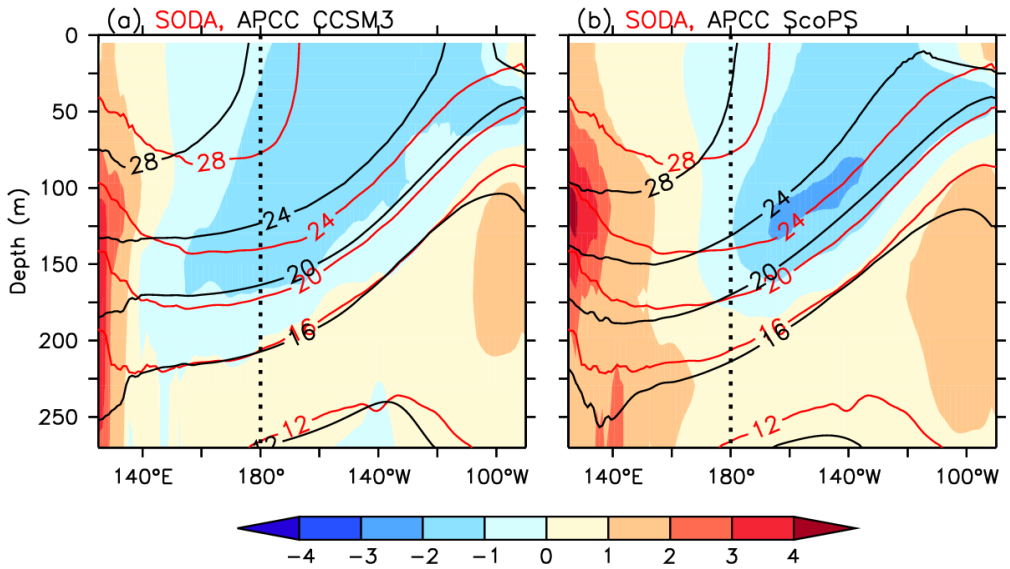

Figure 3 Annual mean Pacific Ocean temperatures (°C) along the equator. Red contours are for the SODA reanalysis and black contours are for the simulated values from the APCC (a) CCSM3 model and (b) SCoPS model. Shades indicate the mean temperature bias of the models against the SODA reanalysis data.

The simulated thermocline (here, its depth is defined as the depth of the 20°C isotherm) in the models is shallower than that observed in the central-to-eastern Pacific Ocean. The CCSM3 model seems to give a correct zonal slope for the thermocline; but the zonal slope simulated in the SCoPS model, which has warmer subsurface ocean temperatures in the western Pacific and colder in the central Pacific than the CCSM3 model, is slightly smaller than the SODA data.

3.1.4 Precipitation

Figure 4a-d shows the observed and simulated annual mean rainfalls over the tropical Pacific region. Both models can capture two clear rain band regions, such as the ITCZ that is elongated zonally from the equatorial western Pacific to the west coasts of Central America and the South Pacific Convergence Zone (SPCZ) that extends from the equatorial western Pacific Ocean southeastward to near the International Dateline as shown in the observations. However, both models have precipitation that is too strong in those rain band regions, which is coincident with

a strong warm bias in the north and south Pacific (See Fig. 1). This "double ITCZ" problem is a common bias in other coupled models (Lin, 2007). There have been a number of studies that reveal the causes of the problem. The error could be due to cloud biases over the South Pacific Ocean (Hwang and Frierson, 2013; Li and Xie, 2014), or it could be associated with errors in the tropical deep convection (Zhang and Wang, 2006; Hirota et al., 2011; Wang et al., 2015).

Nevertheless, the SCoPS model simulates the observed spatial pattern of rainfall better than the CCSM3 model according to pattern correlation (0.75 for the SCoPS model and 0.66 for the CCSM3 model) analysis. Furthermore, the zonal mean rainfall in the CCSM3 model shows a strong north-south symmetric feature against the equator unlike the observations showing that the rainfall in the north is stronger than in the south (Fig. 4d). The symmetric feature becomes weaker in the SCoPS model.

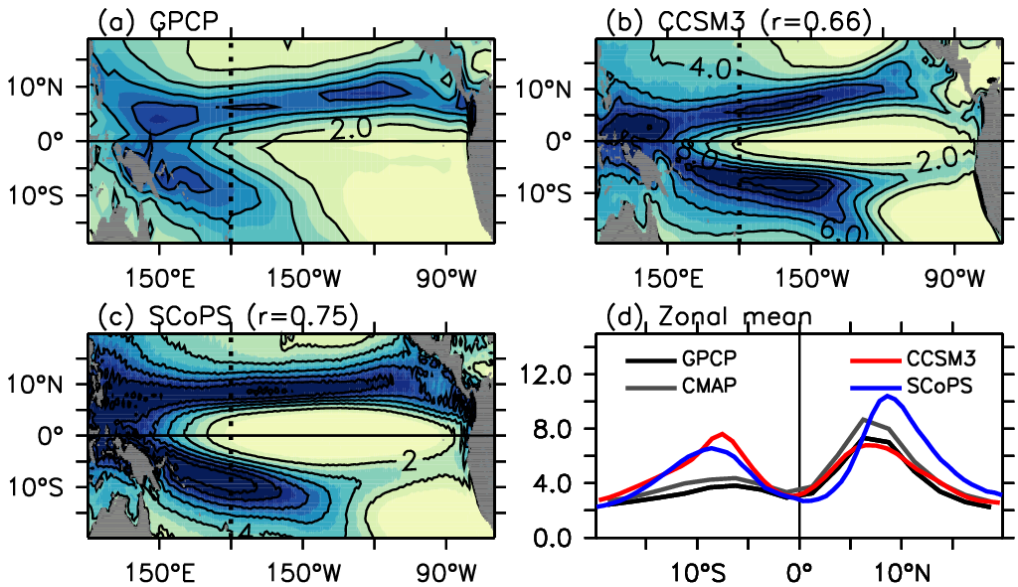

Figure 4 Annual mean precipitation (C.I.=2mm day^{-1}) from (a) GPCP data and (b, c) coupled models; and (d) zonally-averaged (120°E-80°W) precipitation. In b and c, the pattern correlation coefficient between coupled models and the GPCP is shown.

3.1.5 Seasonal Cycle

Figure 5 shows the seasonal cycle of SST and wind stress along the equator from the observations and the models. The observed SST is characterized by an annual cycle in the west, a semi-annual cycle in the east, and a westward propagation of warm water from January to July. The observed SST in the east starts being anomalously cold in July, and the cold anomaly persists until December and reaches its peak during the fall season. Those observed features of the SST annual cycle fail to be simulated by the CCSM3 model. However, the SCoPS model has qualitative agreement with the observations, although the seasonal cycle amplitude is weaker and a peak time of the positive SST anomaly is shifted by one month. The better agreement in the SCoPS model results in a seasonal cycle of wind stress that more resembles the observations, since the SST and the wind are coupled strongly in the tropical Pacific Ocean.

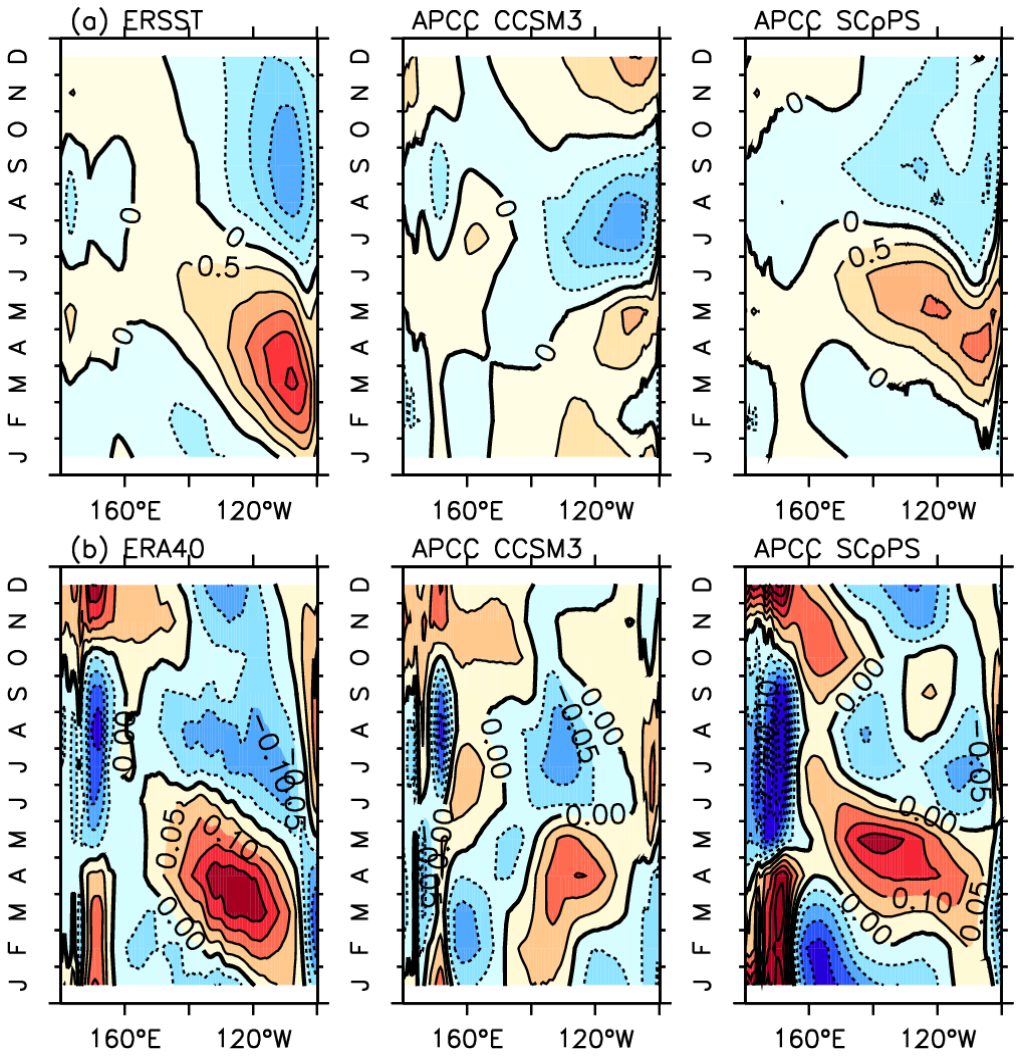

Figure 5 Annual cycle of (a) SST (C.I. = 0.5°C) and (b) wind stress (C.I. = 0.1 dyne cm^{-2}), which are averaged along the equator (2°N-2°S). The left panels are for the observations corresponding to the annual cycle from ERSST and ERA40, and the middle and right panels are for the coupled models.

When the seasonal cycle of the SST is computed with zonal averages in the eastern Pacific, it can be found that the seasonal biases in precipitation are tied to those in the SST as shown in Figure 6. For the observations (Fig. 6a), it is found that the double ITCZ briefly occurs in March-April, when the Northern Hemisphere ITCZ is weakest and precipitation is almost symmetric about the equator. In the boreal summer and fall seasons, when the ITCZ is strongest and the SST reaches

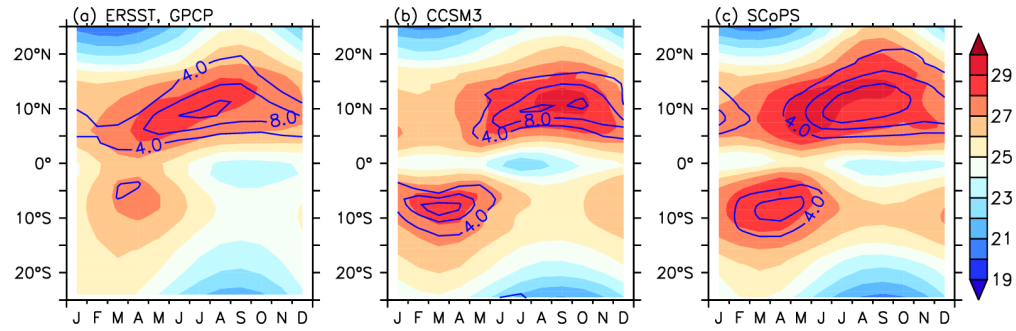

Figure 6 Annual cycle of SST (shades) and precipitation (contours; C.I. = 4.0 mm d^{-1}) averaged zonally over the eastern Pacific (140°W-90°W) from (a) observations and (b, c) coupled models. The name of the models and observations are indicated.

its peak, the observed maximum rainfall occurs in the northern ITCZ. However, both models seem to have an alternating ITCZ error (de Szoeke et al., 2008). That is, in February-May, there is too much strong rainfall south of the equator, where SST is 2°C too warm. Subsequently, the SST and the rainfall peaks occur during the boreal summer and fall seasons in the Northern Hemisphere. This error is known to be tied to the meridional wind bias at the equator (Wittenberg et al., 2006; de Szoeke et al., 2008).

3.2 Tropical Pacific SST variability

3.2.1 Spatial Patterns

To compare the simulated ENSO with the observed one, the first leading empirical orthogonal function (EOF) mode of the interannual SST anomalies over the tropical Pacific are computed from each model and the ERSST as shown in Figure 7. The variance explained by the first leading EOF accounts for more than 40% of the total interannual variance in the observations and in both models. The spatial patterns of the EOF mode from both models are qualitatively in good agreement with those from the observations where a maximum variability in the interannual SST anomalies resides in the eastern equatorial Pacific. The meridional width of the ENSO is improved in the SCoPS model (Fig. 7e), which makes it possible for the pattern correlation of the observed ENSO SST to be larger with the SCoPS model. However, the SST variability in both models is shifted to the west and is extended too far westward with respect to the observations (Fig. 7d).

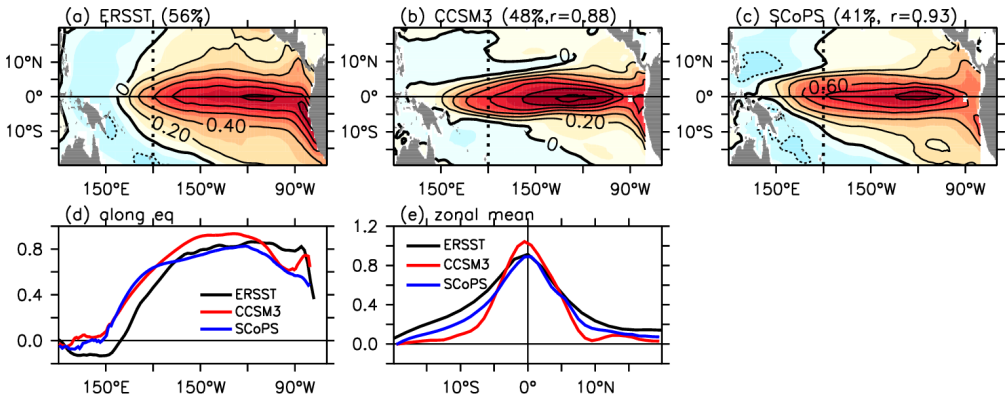

Figure 7 Spatial structure of the first Empirical Orthogonal Function (EOF) mode for SST anomalies from (a) ERSST and (b, c) coupled models; and the modes averaged (d) zonally and (e) along the equator (averaged over 2°N-2°S). In a-c, the percentage of the total variance explained by the leading mode is shown in brackets.

The spatial patterns of atmospheric response and oceanic response to the SST change associated with the ENSO in the tropical Pacific Ocean from the coupled models and the observations are then evaluated. Anomalous precipitation, surface zonal winds, and oceanic heat contents are regressed against the time series of the first principal component (PC) of the tropical Pacific SST anomalies. Here, the time series of the PC is used as a proxy for the temporal evolution of the simulated and observed ENSO.

As for the rainfall response (Fig. 8), the observed rainfall increases along the equator with its anomalies centered near the International Dateline due to the eastward shift of the tropical deep convection region during the El Niño, while dry conditions are prevalent around maritime continents and along 10°N. In the eastern Pacific, the rainfall response is asymmetric about the equator. The spatial pattern of the rainfall anomalies associated with the ENSO indicates that the ITCZ and the SPCZ are merged toward the equator during the El Niño events with respect to its climatology (see Fig. 4). Both models overall seem to capture the observed features. However, some discrepancy is found in both models. The rainfall response is shifted too far to the west in the SCoPS, with the maximum rainfall response located over the western tropical Pacific. This could result from the overly warm western tropical Pacific that likely makes the rainfall response too sensitive to the SST change and from the penetration of the cold tongue into the central Pacific that makes the response

confined in the western Pacific (See Fig. 1). The CCSM3 model shows the rainfall response to be too meridionally symmetric in the eastern Pacific, probably due to the overly warm SST bias in the central south tropical Pacific (see Fig. 1e and f), while the SCoPS model better captures the observed meridional asymmetric feature of the rainfall response.

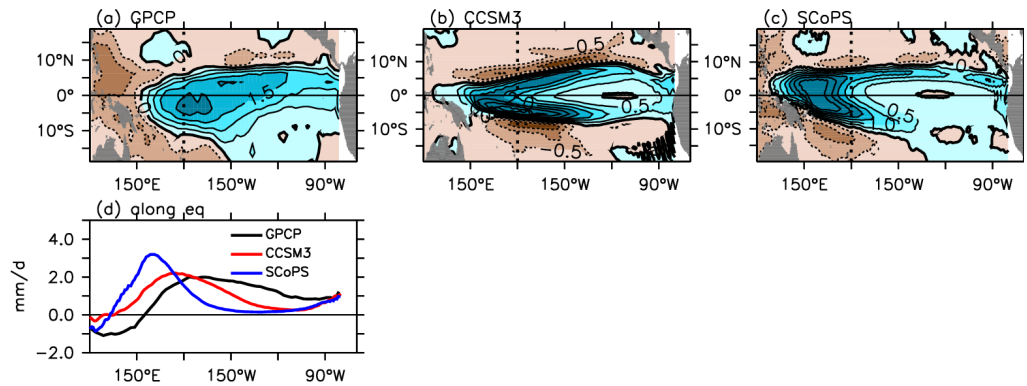

Figure 8 Precipitation anomalies (C.I. = 0.5 mm d^{-1}) regressed against the time coefficients of the first EOF mode for anomalous SSTs from (a) observations, (b, c) coupled models, and (d) the zonally averaged regression coefficients from (a)-(c). Observations correspond to the first principal component from the ERSST V2 reanalysis and rainfall anomalies are from the GPCP analysis.

The response of the zonal wind stress anomalies to the interannual SST anomalies in the models and observations is shown in Figure 9. The observations show westerly wind anomalies in the central equatorial Pacific region during warm events with its peak placed slightly to the east of the International Dateline. The zonal location of the wind response is captured better by the CCSM3 model than the SCoPS model, where the westerly wind response to the equatorial Pacific SST anomalies during the ENSO is shifted to the far west compared to the observations. The meridional extent of the response is better captured by the SCoPS model while the meridional extent from the CCSM3 model is too narrow (Fig. 9d).

Figure 10 displays the response of anomalous oceanic heat contents during the El Niño from the simulations and the SODA ocean reanalysis data. The heat content anomalies are usually used as a proxy for the change in the equatorial Pacific thermocline depth. The response of the heat content anomalies taken from the SODA data has a zonal dipole structure, with the anomalies of opposite signs at the eastern and western sides of the tropical Pacific, indicating a change in the zonal

slope of the equatorial thermocline. That is, during the El Niño, the SODA reanalysis data show a deepened thermocline in the eastern Pacific with its peak along the equator and an elevated thermocline in the western Pacific with its peaks around 7°N and 7°S. The deepened thermocline is related to reduced equatorial easterly winds and the equatorial downwelling Kelvin waves; whereas, the elevated thermocline is associated with enhanced positive wind curls and off-equatorial upwelling Rossby waves due to the development of anomalous westerly winds in the western Pacific during a warm event. Qualitatively, both models have thermocline response patterns that are in a good agreement with that of the ocean reanalysis data. The pattern correlation coefficients between the models and the reanalysis data are greater than 0.8.

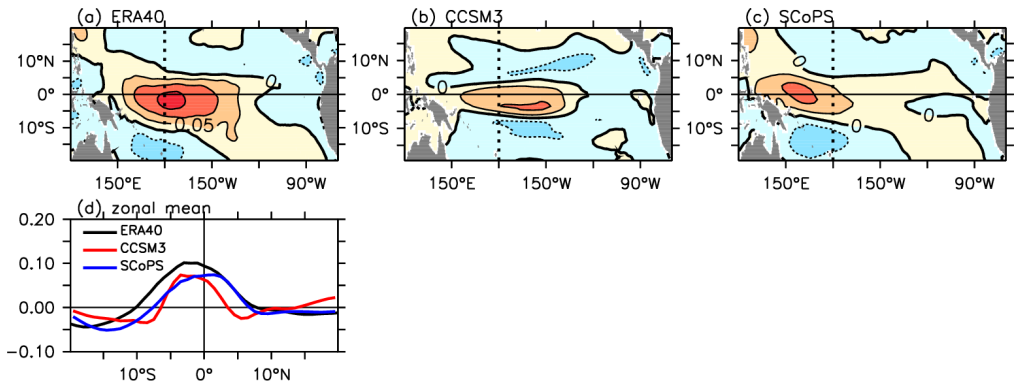

Figure 9 Wind stress anomalies (C.I. = 0.05 dyne cm^{-2}) regressed against the time coefficients of the first EOF mode for anomalous SSTs from (a) observations, (b, c) coupled models, and (d) zonally-averaged (130°E-150°W) regression coefficients from (a)-(c). For the observed wind stress, we use ERA40 data.

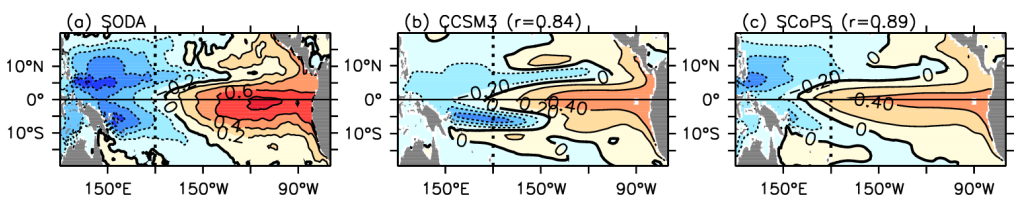

Figure 10 Heat content anomalies regressed against the time coefficients of the first EOF mode for anomalous SSTs from (a) observations and (b, c) coupled models. For the observed heat contents, we use SODA reanalysis data. The heat contents are defined as the ocean temperatures vertically averaged from the ocean surface to a depth of 300m. In b and c, pattern correlation coefficients between the SODA data and the models are indicated.

3.2.2 Temporal Patterns

Figure 11 shows the lag regression patterns of the equatorial SST anomalies, the zonal wind stress anomalies, the anomalous zonal currents, the ocean heat content anomalies along the equator, and the zonally averaged ocean heat content anomalies against the first PC of the SST anomalies as a function of longitude (latitude for zonally averaged ocean heat content anomalies) and phase lag from the observations and both models.

In Figure 11a, the observed warm SST anomalies, which exhibit a stationary growth elongated from the western Pacific to the far eastern Pacific, start to grow earlier in the western region of the equatorial Pacific basin than in the eastern region, while cold anomalies occur in the far western Pacific during the development of the observed warm event. Furthermore, the observed cold SST anomalies in the eastern Pacific appear about 9 to 10 months after and before the warm event peak. Overall, the SCoPS model appears to better capture the observed ENSO SST evolution than does the CCSM3 model. In the CCSM3 model, the warm and cold events are too brief relative to the observations and the SST anomalies show an exaggerated westward propagating signature. This figure implies that the CCSM3 model simulates the ENSO with a timescale that is too short (about 2 years) relative to the observations where the ENSO has dominant periods of about 3-5 years. An overly short ENSO period in the CCSM3 model may be partly related to the meridionally narrower wind response (Fig. 9), which will excite fast off-equatorial Rossby waves (An and Wang, 2000).

In Figure 11b, the observed zonal wind stress anomalies show a clear eastward-propagating signature, with anomalous westerly winds in the far west appearing about 12 months prior to a warm peak. The maximum observed westerly wind anomaly occurs in the central Pacific (near the International Dateline) about 1 to 2 months before the warm peak, while simultaneously anomalous easterly winds start growing on the far western side of the equatorial Pacific Ocean. These observed features are captured more closely by the SCoPS model, although there are differences in its simulation of the location of the peak of westerly wind anomalies and the strength of the wind response to an ENSO SST anomaly in comparison to the

observations. The CCSM3 model has westerly wind anomalies that propagate slightly westward, which may be related to its strong westward propagating SST bias.

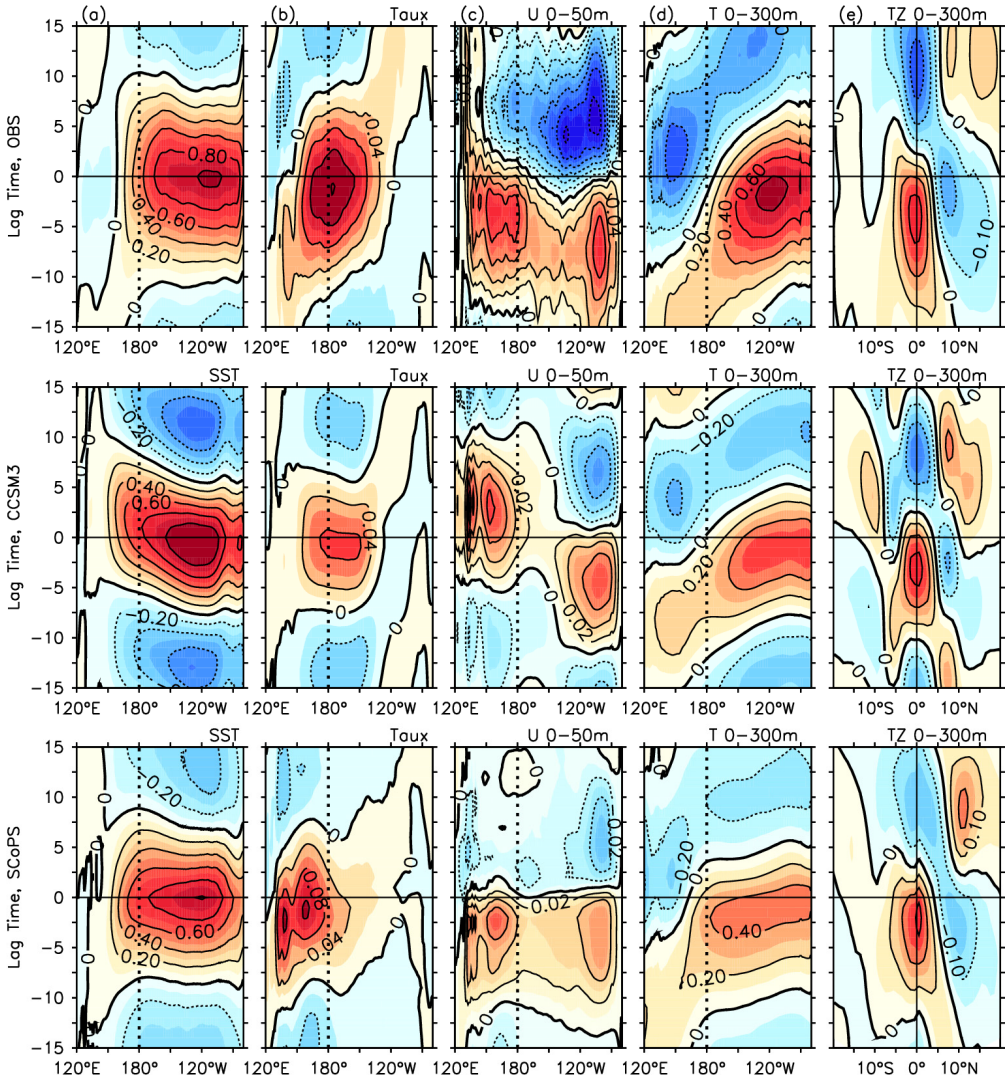

Figure 11 Lag regressions of interannual equatorial (a) SST (C.I. = 0.2 °C), (b) wind (C.I. = 0.04 dyne cm^{-2}), (c) upper layer (0-50m average) zonal currents (C.I. = 0.02 m sec^{-1}). (d) heat content anomalies (C.I. = 0.2 °C) averaged along the equator, and (e) zonally averaged heat content anomalies (C.I. = 0.2 °C), from left to right panels, against the time coefficients of the first EOF mode of the ENSO SSTs from observations (upper panels) and coupled models (middle and lower panels). Model names are indicated on the left side of each panel. Lag-0 indicates a peak of a warm event, positive lags correspond to the anomalies lagging the first principal component in time, and negative lags correspond to the anomalies leading the first principal component in time.

The peak in near-surface eastward zonal current anomalies associated with the ENSO in the SODA reanalysis data (Fig. 11c) occurs about 5 to 10 months prior to a warm peak in the far eastern Pacific and the western Pacific. On the other hand, anomalous westward zonal currents in the eastern equatorial Pacific region start developing around the warm event peak and reach their peak about 5 to 10 months after the warm peak. The lag relationship is captured very well by the SCoPS model, although its response strength is too weak in the model. The nearly quadrature relationship between the anomalous surface currents and the first PC of the ENSO SST anomalies suggests that the anomalous zonal currents contribute to not only the ENSO growth but also its phase transition through advecting the climatological mean SST (An and Jin, 2001; Jin and An, 1999; Picaut et al., 1997) in both the reanalysis data and the SCoPS model. However, in the CCSM3 model, the anomalous eastward currents in the west begin developing around a warm peak; and there is a strong westward propagation of the anomalous zonal currents, which is not discernable in the SODA reanalysis data. The strong westward-propagating anomalous zonal currents in the model may be partly responsible for the strong westward-propagating signature in the equatorial SST anomalies.

As shown in Figure 11d, positive equatorial ocean heat content anomalies propagate from west to east during a development of the El Niño with a reduced slope of equatorial thermocline at the El Niño peak. A maximum in the deepening of the thermocline depth in the eastern equatorial Pacific is reached about 2 to 5 months prior to the El Niño peak. In general, both models capture the observed features qualitatively, although their simulated thermocline response is weaker.

Figure 11e shows that the zonal-mean heat contents along the equator increase during the El Niño development and decrease during its decay in both models and in the SODA reanalysis data, which depicts the recharge/discharge process of the equatorial heat contents (Jin, 1997). The equatorial heat contents have peaks at 3 to 5 months prior to the El Niño peak accompanied by a deficit in the heat contents along 5°N-10°N. About 10 to 15 months after the peak, the opposite occurs; that is, there are negative heat content anomalies along the equator and positive heat content anomalies along 5°N-10°N. The recharge/discharge process seems to be captured better by the SCoPS model.

3.2.3 Seasonal Phase Locking

Figure 12 shows the standard deviation of the interannual SST anomalies averaged over the Niño 3.4 region from the ERSST and the coupled models as a function of calendar month. In the ERSST data, there is a maximum in the standard deviation during the winter and a minimum during the spring season, which suggests that the El Niño tends to have a peak around the end of the calendar year. Overall, this observed phase-locking feature can be simulated with both coupled models, although the maximum standard deviation in the winter season is much smaller in the SCoPS model and there is a difference of about one month in the timing of the minimum standard deviation in both models compared to the ERSST data.

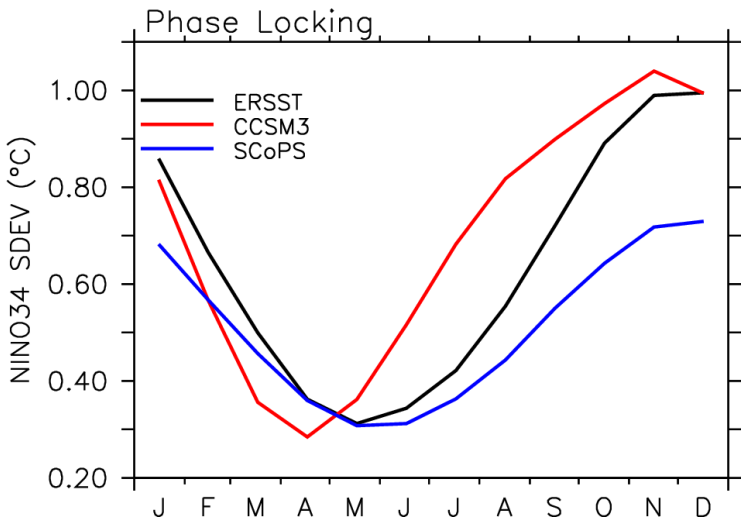

Figure 12 Phase-locking feature of the ENSO from the ERSST data and the coupled models. The phase-locking is estimated with the standard deviation of the Niño 3.4 index in each calendar month.

3.2.4 ENSO Stability

Figure 13 shows the ENSO feedbacks and the ENSO stability as estimated with the BJ index analysis. The thermocline feedback is the primary contributor to the observed ENSO growth, and the zonal-advective feedback plays a secondary role in growing the tropical Pacific SST variability. Among the negative feedback terms that tend to decay the observed ENSO, the thermodynamic damping term is the most dominant. According to the BJ index, the observed ENSO (BJ = -0.21 yr^{-1}) is a damped mode of the atmosphere-ocean coupled system that is sustained by atmospheric stochastic forcing (Wang and Picaut, 2004). The ENSO simulated in both models is also a damped mode (-0.31 for the CCSM3 model and -0.73 for the SCoPS model). However, the ENSO stability derived from the coupled models is a result of some biases in the feedback terms. In the CCSM3 model, the relative contribution of the feedback terms to the ENSO growth is similar to the reanalysis data, but they are underestimated. The underestimation is large in three positive feedback terms and in the thermodynamic damping. A similar situation for the underestimation also occurs in the SCoPS model except for the Ekman feedback and mean advection damping, which have magnitudes close to the observations. The error in thermodynamic damping is improved in the SCoPS model compared to the CCSM3 model. The underestimation of the positive feedback terms in the CCSM3 model tends to be offset by an overly small thermodynamic damping leading to the ENSO stability, as estimated with the BJ index that is close to the observations. Due to this error cancellation effect, the CCSM3 model may provide a more correct value of the ENSO stability (and also the ENSO amplitude—the difference from the observations is 0.08°C for the CCSM3 model and 0.11°C for the SCoPS model), but for the wrong reasons. The underestimation of the feedback terms in both models is known to be partly due to the equatorial cold tongue bias, which is prevalent in both models (Kim et al., 2014).

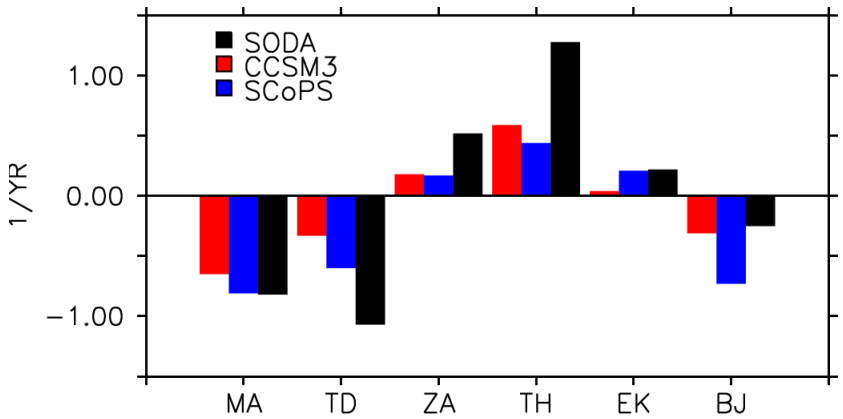

Figure 13 Feedback terms comprising the BJ index from observations and coupled models: MA stands for mean advection damping, TD for thermodynamic damping, ZA for zonal advective feedback, TH for thermocline feedback, EK for Ekman feedback, and BJ for BJ index.

3.3 ENSO Teleconnections

3.3.1 Geopotential Height at 200 hPa

For displaying the ENSO related atmospheric circulations in the coupled models and observations, the regressed patterns of the winter season (DJF average) 200mb geopotential height against the time series of the PC of the tropical Pacific SST variability are obtained as shown in Figure 14. From the observations, we can identify the wave train pattern where two high centers are located over the eastern equatorial Pacific and Canada and two low centers over the extratropical eastern Pacific and the southern U.S. These winter atmospheric teleconnection patterns have been discussed in a number of previous studies (e.g., Horel and Wallace, 1982; Alexander et al., 2002).

In general, both models can capture the wave train pattern, although there is a slight difference in the location of the wave centers and the wave amplitudes. Both models have stronger amplitudes than those observed over Canada and the southern US, although the amplitudes of the equatorial Pacific anomalies are too small relative to the observations. The anomalies over the extratropical Pacific Ocean and over Canada are shifted to the west in both models, relative to the observations. The westward shift is slightly larger in the SCoPS model with respect to the CCSM3 model, which

may be related to errors in the response of the tropical Pacific precipitation to the ENSO (see Fig. 8). The low height center over the southern U.S. from the reanalysis data, which is captured better by the SCoPS model, is located over the southeastern region of the U.S in the CCSM3 model. In the observations, there also exist two weak wave centers over East Asia, with a high center located over the Korea-Japan region and a low center over southern China. This feature is also simulated better in the SCoPS model. The errors in the locations of the wave trains strongly affect the simulations of the ENSO related precipitation over the mid-latitude countries (Hoerling and Kumar, 2002; Cai et al., 2011) as can be identified in next section.

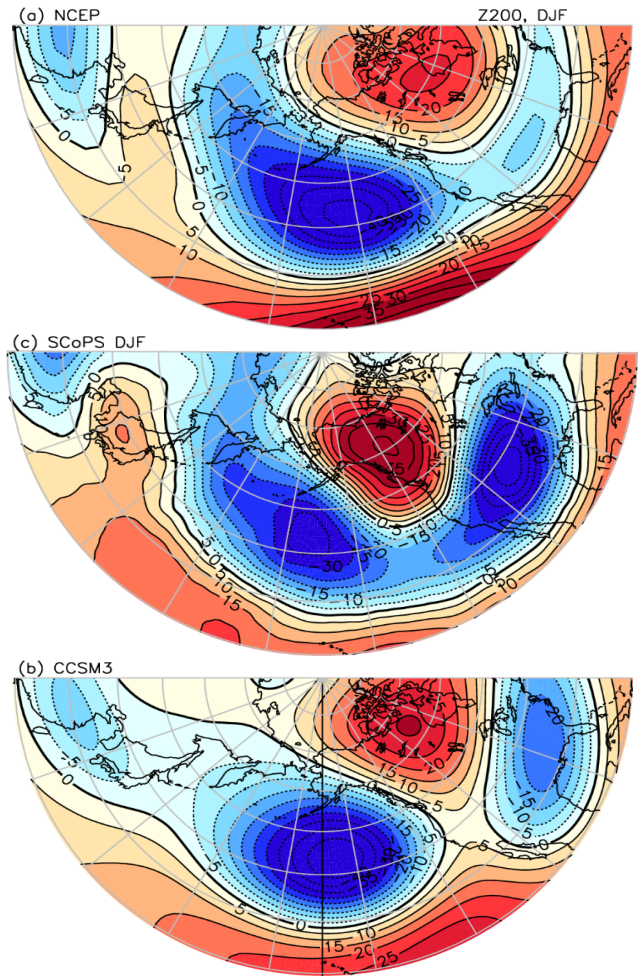

Figure 14 The 200 hPa geopotential height anomalies (m, DJF average) regressed against the time coefficients of the first EOF mode for anomalous SSTs from (a) ERSST and (b, c) coupled models. The observed geopotential height is taken from the NCEP reanalysis data.

3.3.2 Precipitation

Figure 15 shows the seasonal stratification (JJA and DJF average) of the relationship of global precipitation with the ENSO mode. As indicated in the observations (Fig. 15a and b), the precipitation condition in the south Asian monsoon regions changes with the El Niño phases and the seasons. That is, during a developing El Niño phase (i.e., summer season, JJA) there is tendency towards dry conditions over India, while during mature El Niño phases (i.e., winter season, DJF) there is a tendency towards wet conditions over the northern part of India, the west Indian Ocean, and southeast Africa. The JJA dryness may be related to the weakening of the south Asian monsoons since the ENSO forced Indian Ocean warming tends to decrease land-ocean thermal contrasts (Klein, 1999). The DJF wet tendency may be due to ascending moisture and air associated with the warmer SST in the western Indian Ocean and easterly wind anomalies across the Indian Ocean. Both models can capture the JJA El Niño impact on the Indian rainfall, but they fail to simulate the observed El Niño impact during the DJF season.

In observations, the El Niño impact on the East Asian rainfall is not clear during JJA season, but there is some indication of enhanced rainfall over southeastern China and the Korean Peninsula during the winter season. The increase in the East Asian winter rainfall is related to the anomalous anticyclonic circulation near the surface over the western North Pacific (near the Philippine Sea) during the mature El Niño phase (Wang et al., 2000). The East Asian winter rainfall change during the El Niño events is better simulated by the SCoPS model, which may be due to the teleconnection patterns near the East Asian region that have closer agreement with the observations (see Fig. 14a and c).

The observed US rainfall change during El Niño events is characterized by wet conditions in the north and dry conditions in the south over the eastern region in JJA, which are not captured by both models. The observed wet condition over the southern US in DJF can only be captured by the SCoPS model that can simulate better the observed teleconnection wave center over the southern US. The observed DJF dry conditions over the Amazonian region, the maritime continents, and northern Australia during the El Niño events are simulated better with the SCoPS model.

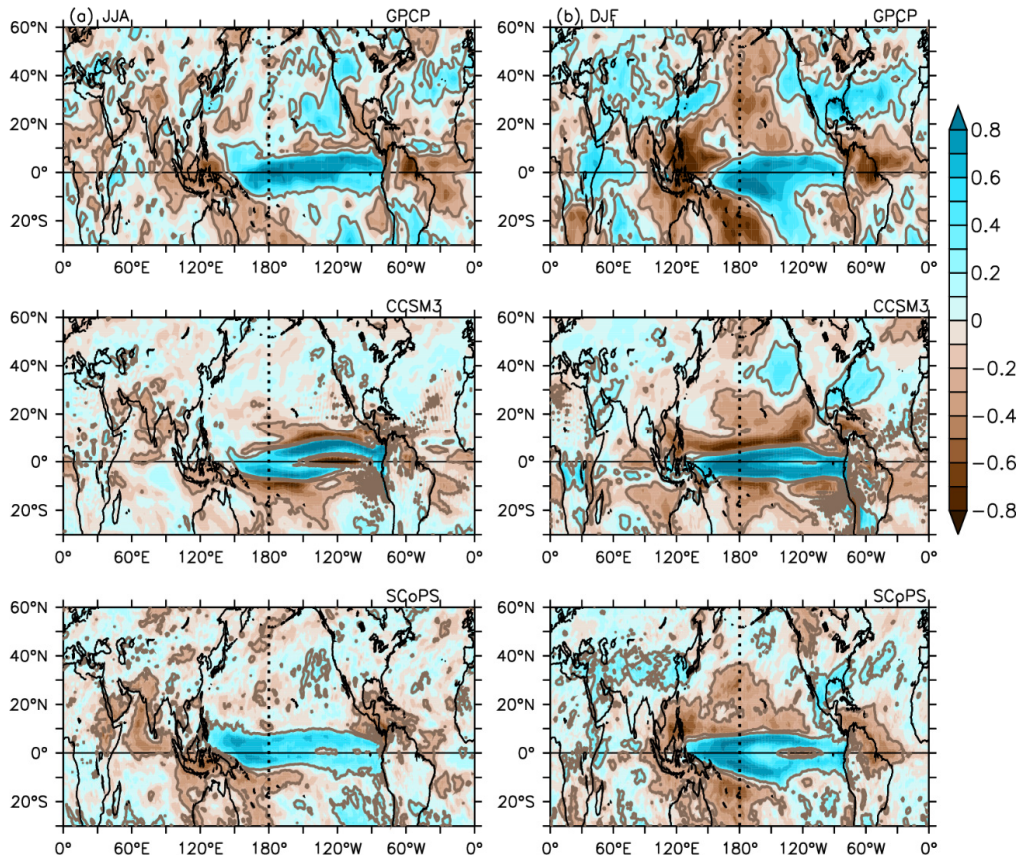

Figure 15 Spatial patterns of correlation coefficients between precipitation and the time coefficients of the first EOF mode for anomalous SSTs from observations (upper panels), CCSM3 model (middle), and SCoPS model (lower). The observed SSTs and precipitation are taken from the ERSST and GPCP datasets, respectively. The correlation coefficients are estimated based on JJA (left) and DJF (right) average. Brown-colored contour lines correspond to the correlation coefficients significant at the 90% level for a 200 year coupled run.

4. ASSESSMENT OF PREDICTION SKILL OF THE TROPICAL PACIFIC CLIMATE

4.1 Improvement of Prediction Skill from the GODAS to the GODAS-Nudging Method

4.1.1 ENSO Prediction

Figure 16 shows the TCC between the observed and predicted Niño 3.4 indices. With early lead times, namely, 0- and 1-month lead times, the prediction skill of the Niño index is improved when the GODAS nudging method is applied for generating initial conditions. Particularly, the TCC is slightly larger (0.9 for the GODAS nudging and 0.87 for the GODAS method) and the RMSE is decreased from 0.48 to 0.42 in the GODAS nudging method at 1-month lead time. The TCCs gradually decrease with an increase in the forecast lead months and reach about 0.6 at 6-month leadtime for both methods (Fig. 16c). This indicates that the good predictions for the interannual ENSO events can be made by the CCSM3 model at least over a 6-month lead time, even with the simple initialization methods. It is also found that the predicted ENSO amplitude that is closer to the observed one (0.92°C) with the GODAS nudging method persisting until a 4-month lead time, whereas the ENSO amplitude (0.61°C) predicted with the GODAS method is too small even at a 1-month lead time. Moreover, predictions with the GODAS method have larger RMSE at the 0- and 1-month lead times. During early lead times, the larger RMSE and the weak ENSO strength from the predictions with the GODAS method may be due to initialization shock. The problem seems to be solved with the GODAS nudging method.

Figure 17 shows the seasonal dependence of TCC and RMSE for the ENSO prediction and indicates that for both initializations, TCC decreases quickly with increasing lead times when the predictions are initialized in the winter and early spring seasons (December to March). For example, when starting from the month of January, the TCC is already decreased below 0.4 in predictions with the GODAS method at the 4-month lead time. This is partly related to the well-known “spring barrier” problem that the ENSO persistence and predictability decrease rapidly in

spring season (e.g., Webster and Yang, 1992). The rapid decrease problem is improved with the GODAS nudging method, where a TCC larger than 0.5 is maintained until the 4-month lead time. With both initialization methods, the TCC decrease rate with lead times is reduced towards November, and good predictions can be achieved, with TCC values larger than 0.7 being sustained throughout 6-month lead times when the predictions start by June or July. The RMSE of the Niño 3.4 index predicted using the GODAS method shows a rapid increase when the predictions are initialized in late winter (January-March) and summer (June-August). The rapid increase problem is also improved in the GODAS nudging method (Fig. 17d and f).

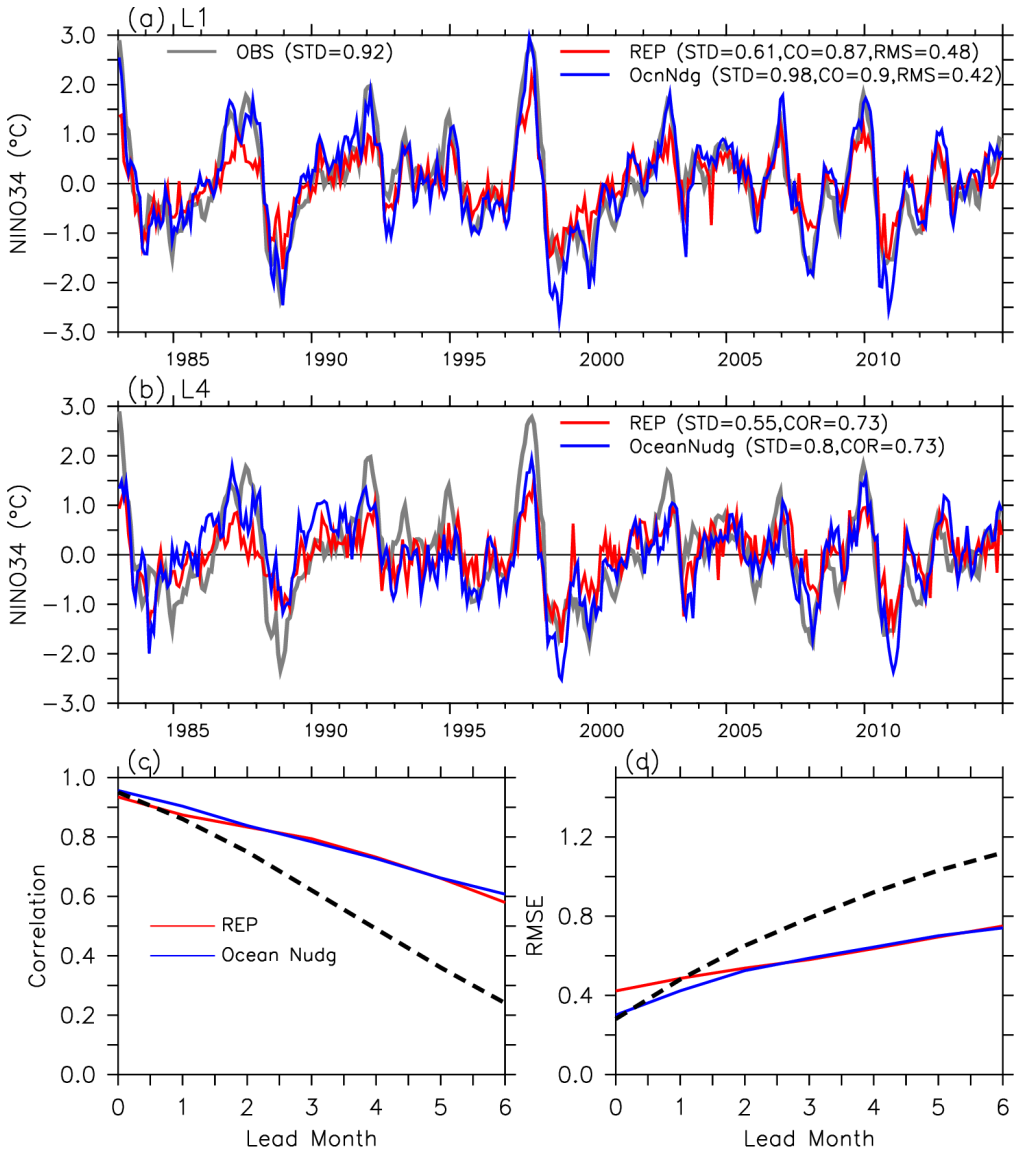

Figure 16 Time series of the Niño 3.4 index (°C) from observations (gray line) and predictions (red line for GODAS method and blue for GODAS nudging method) at (a) 1-month lead time and (b) 4-month lead time; and (c) TCC and (d) RMSE between the observed and predicted Niño 3.4 indices from 0- to 6-month lead times.

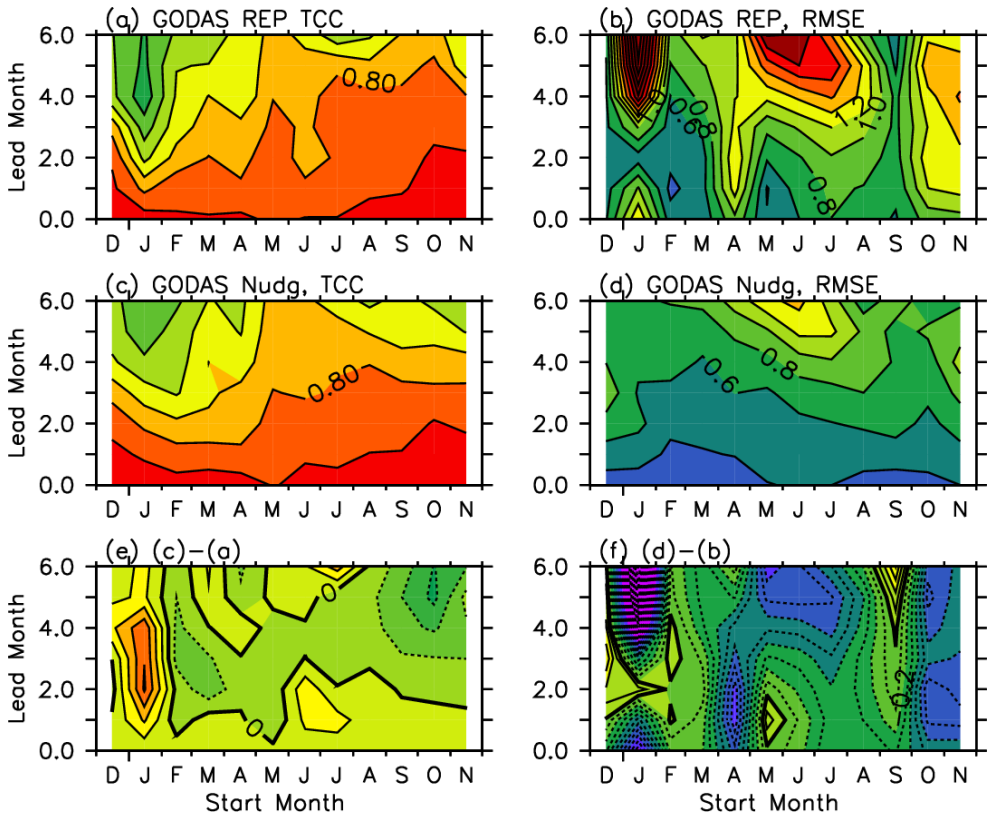

Figure 17 Seasonal stratification of the TCC (left panels) and RMSE (right panels) of the predicted Niño 3.4 index using (a, b) the GODAS initialization method and (c, d) the GODAS nudging method with respect to the observations; and the difference in (e) TCC (C.I. = 0.05) and (f) RMSE (C.I. = 0.1 °C) between both methods.

4.1.2 Global Climate

In Figure 18, which displays TCCs at grid points between the observed and predicted global ocean SST, it is identified that there is improved skill in predicting the global ocean SST with the GODAS nudging method. At a 1-month lead time, the TCC is greater than 0.7 in the south Indian Ocean, the North Pacific Ocean, and the southwest Pacific Ocean (Fig. 18b). The TCC over those regions is still significant at a 95% level at a 4-month lead time (Fig. 18d). However, the predictions initialized with the GODAS method shows that the TCC is below 0.6 at even a 1-month lead time, and the 95%-significant TCCs are not shown over the above-mentioned regions at a 4-month lead time.

As for global precipitation predictions (Fig. 19), the skill score (e.g., TCC) is poor over all of the oceans, even at the 1-month lead time, except for over the equatorial Pacific Ocean. That is, significant TCCs are confined to the equatorial

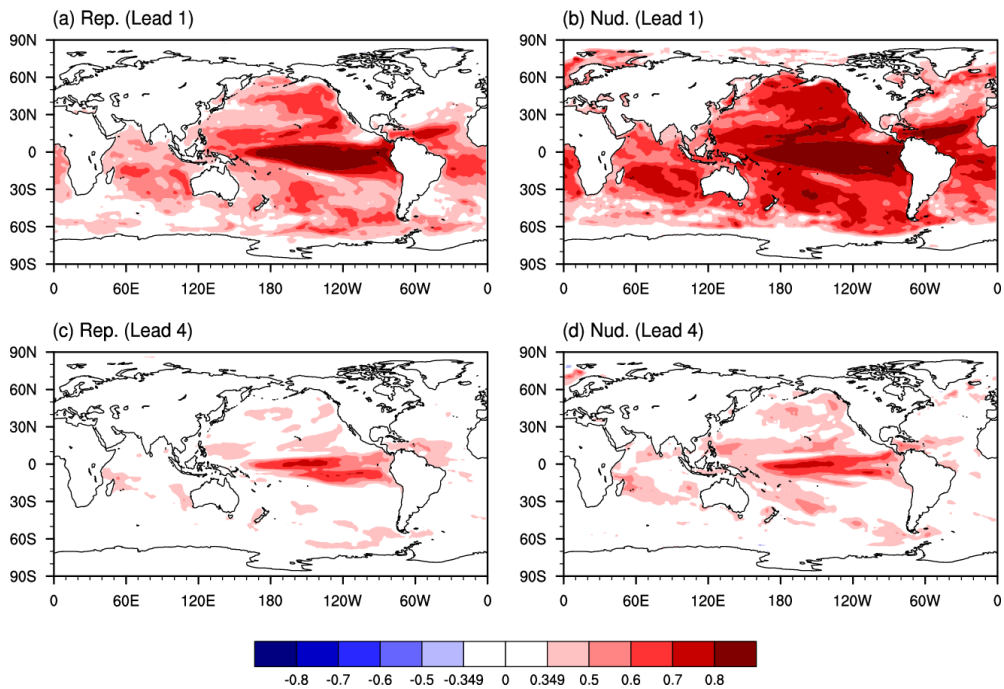

Figure 18 TCCs between observed and predicted SSTs in the global oceans at (a, b) 1-month lead time and (c, d) 4-month lead time. Left panels are for the GODAS method and right panels are for the GODAS nudging method. Only TCCs that are significant at the 95% level are color shaded.

Pacific Ocean for both initialization methods at 1-and 4-month lead times. Furthermore, it seems that the prediction error is not resolved with an improved initial condition, although the GODAS nudging method gives an improved prediction for precipitation in the eastern equatorial Pacific Ocean at a 1-month lead timecompared to the GODAS method.

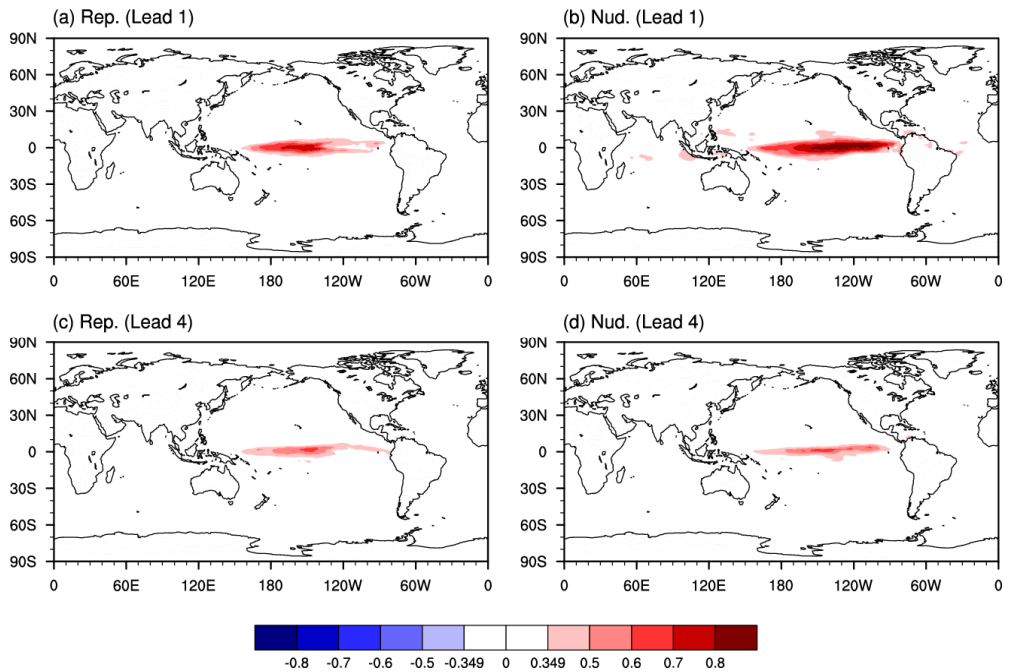

Figure 19 TCCs between observed and predicted precipitation in the global oceans at (a, b) 1-month lead time and (c, d) 4-month lead time. Left panels are for the GODAS method and right panels are for the GODAS nudging method. Only TCCs that are significant at the 95% level are color shaded.

Figure 20 displays the TCCs of the seasonally averaged 2-meter air temperature predicted at a 1-month lead time with that from the NCEP reanalysis and indicates improved predictions using the GODAS nudging method. Strong negative TCCs (> -0.5) over land regions in the predictions for some seasons with the GODAS method [e.g., SON prediction (Fig. 20a and b) over North America and JFM prediction (Fig. 20e and f) over the Eurasian continent], which may severely affect the prediction skill of the APCC MME prediction system, disappear to some extent in predictions using the GODAS nudging method. Although the refined atmosphere and land initializations are not considered (please be reminded that the initial conditions of the atmosphere and the land are determined by their adjustment to the ocean

state during the simple ocean nudging initialization process in a coupled mode), significant correlation coefficients (at 90% level) between predicted air temperature using the GODAS nudging method and the observations are found in some extratropical land regions during some target seasons, such as over the east Asia

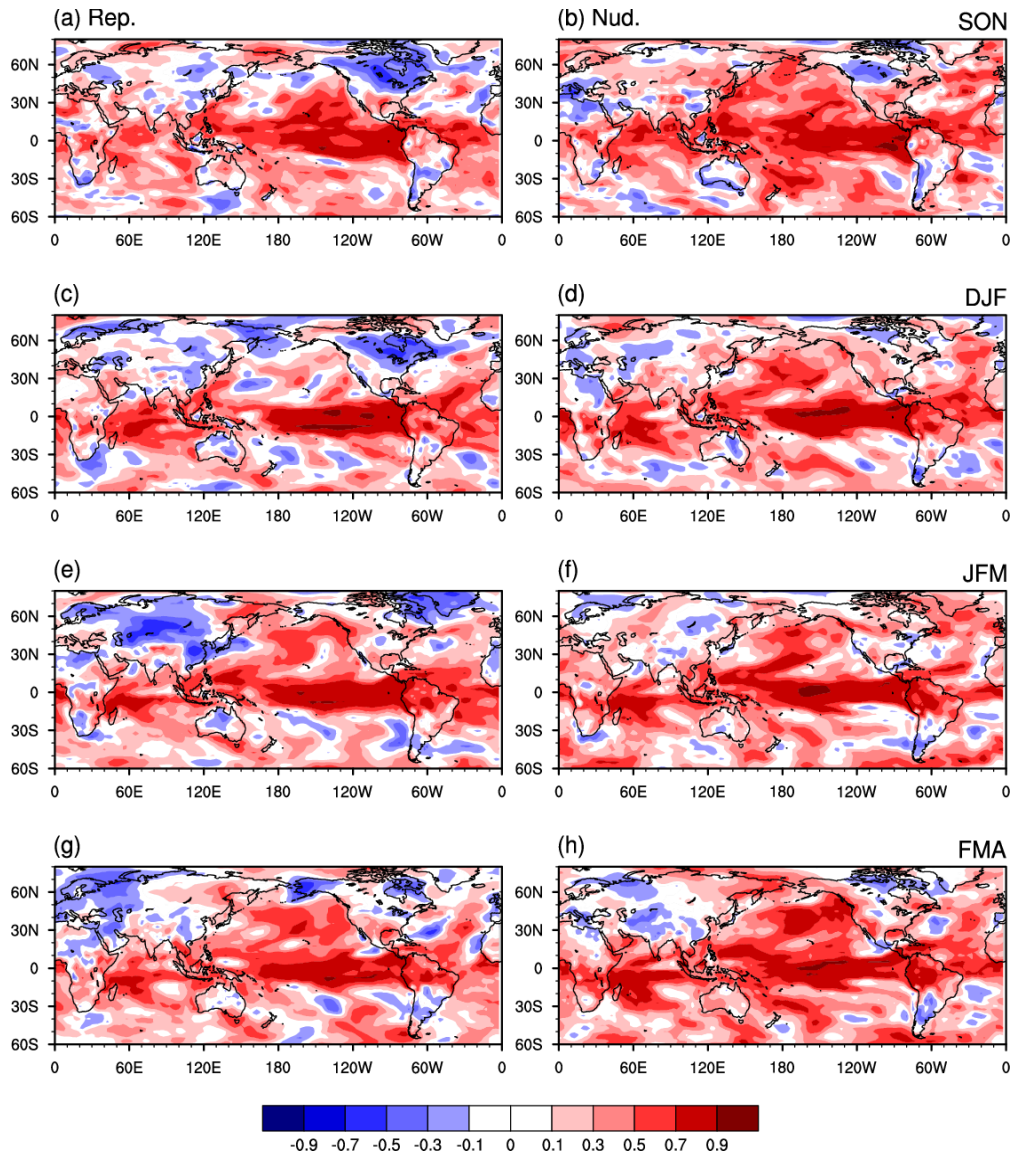

Figure 20 TCCs of 2m air temperatures predicted during the target seasons, namely, (a, b) SON, (c, d) DJF, (e, f) JFM, and (g, h) FMA at a 1-month lead time, with respect to the NCEP reanalysis data. The left panels are for the GODAS method and the right panels are for the GODAS nudging method.

and the southern US in SON forecasts, and the western US in DJF and FMA forecasts. These high correlation coefficients are not found with the GODAS method simulations.

To sum up, it seems that the initialization shock problem in predictions using the GODAS method seems to affect the forecasting of the Niño index and further extratropical air temperatures with short lead times. The GODAS nudging method is able to mitigate the initialization shock and thus improve the overall forecast skills.

4.2 Role of Surface Winds in Initial Conditions

In the tropical Pacific, the important role of the surface winds in the ENSO feedback process is well known (Jin, 1997; Battisti and Hirst, 1989; Fedorov and Philander, 2001). Specifically, it has been argued that westerly wind bursts (WWBs) that occasionally occur in the tropical Pacific warm pool regions play an important role in ENSO dynamics (Vecchi and Harrison, 2000; Lengaigne et al., 2004; Eisenman et al., 2005; Vecchi, 2006; Fedorov et al., 2014; Lian et al., 2014). The WWBs can trigger the ENSO events and modulate the ENSO strength (Lengaigne et al., 2004; McPhaden, 1999). Particularly, consecutive WWBs are known to be responsible for the development of the unusually strong 1997/98 El Niño event. Further, recent studies argued that the WWBs would play some role in diverse ENSO development (e.g., two types of ENSO) (Fedorov et al., 2014; Lian et al., 2014; Chen et al., 2015). The WWBs are mainly linked to various atmospheric circulation conditions, including tropical cyclones (e.g., McBride et al., 1995), the convective episodes related with the Madden Julien Oscillation (e.g., Zhang, 1996), and the cold surges from midlatitudes (e.g., Chu, 1988). The intensity of the WWB can be increased further by its interaction with the ENSO related SST (e.g., Jin et al., 2007). The surface winds driven by atmospheric circulation conditions may not be generated with the GODAS nudging method; and, therefore, random noises like WWBs are difficult to be included in the initial conditions. We, therefore, apply the GODAS-WIND nudging method (see Section 2.3) for generating initial conditions. The results are shown in Figures 21 and 22.

Figure 21 shows the oceanic heat content and SST anomalies along the equatorial Pacific (2°S-2°N) from the GODAS reanalysis data and the initial conditions generated

with the GODAS nudging and GODAS-WIND nudging methods. When compared to the GODAS reanalysis data, both initial conditions show that the simulated anomalous heat content and SST variations have a close resemblance to the observations. We can identify the eastward propagation of the heat content anomalies associated with the ENSO events in both initial conditions, which are comparable to the observations. Therefore, the comparison between the GODAS nudging and GODAS-WIND nudging initialization schemes indicates that there is no discernable contribution of the wind nudging to the structure of the surface and the subsurface ocean temperatures and that both initialization methods can provide realistic oceanic memory for predicting ENSO events.

However, we can clearly identify the enormous contribution of the wind nudging in making the wind initial conditions much closer to the observations in Figure 22

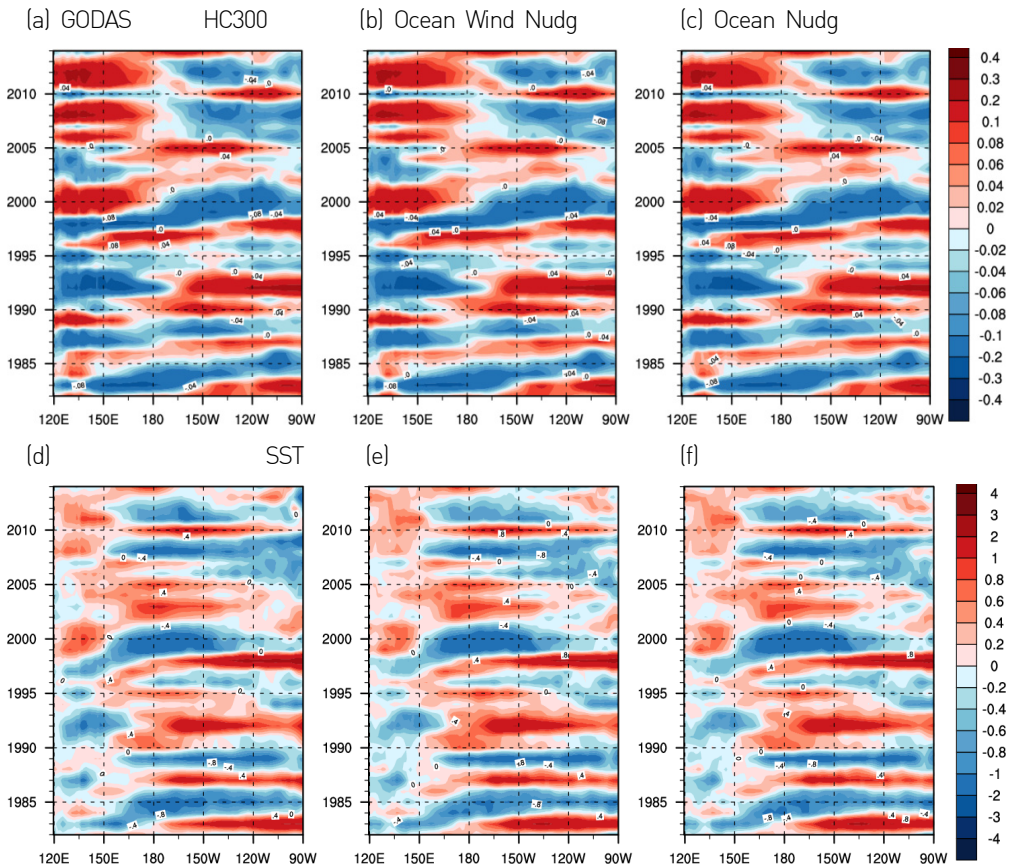

Figure 21 Oceanic heat content (10^{10} J m^{-2}) (upper panels) and SST (°C) (lower panels) anomalies along the equatorial Pacific (2°S-2°N) from (a, d) GODAS reanalysis data and initial conditions generated with (b, e) the GODAS-WIND nudging method and (c, f) GODAS nudging method.

showing surface wind anomalies along the equator. The GODAS-WIND nudging method can capture most observed features of the anomalous surface winds (Fig. 22b and d), whereas the wind anomalies generated with the GODAS nudging method miss many of the observed features (Fig. 22c and e). Furthermore, although observed wind anomalies over the western-to-central equatorial Pacific associated with the ENSO events or the eastern equatorial SST variations can be captured by the GODAS nudging initialization method to some extent, there are significant differences in the intensity of the wind anomalies during the development of major El Niño events. For example, the anomalous westerly winds during 1997/98 and 1991/92 El Niño development are underestimated. The discrepancies of the GODAS nudging method are more prevalent in the eastern equatorial Pacific region. In particular, the GODAS nudging initialization method cannot simulate the observed easterly wind anomalies that persisted during the 1980s.

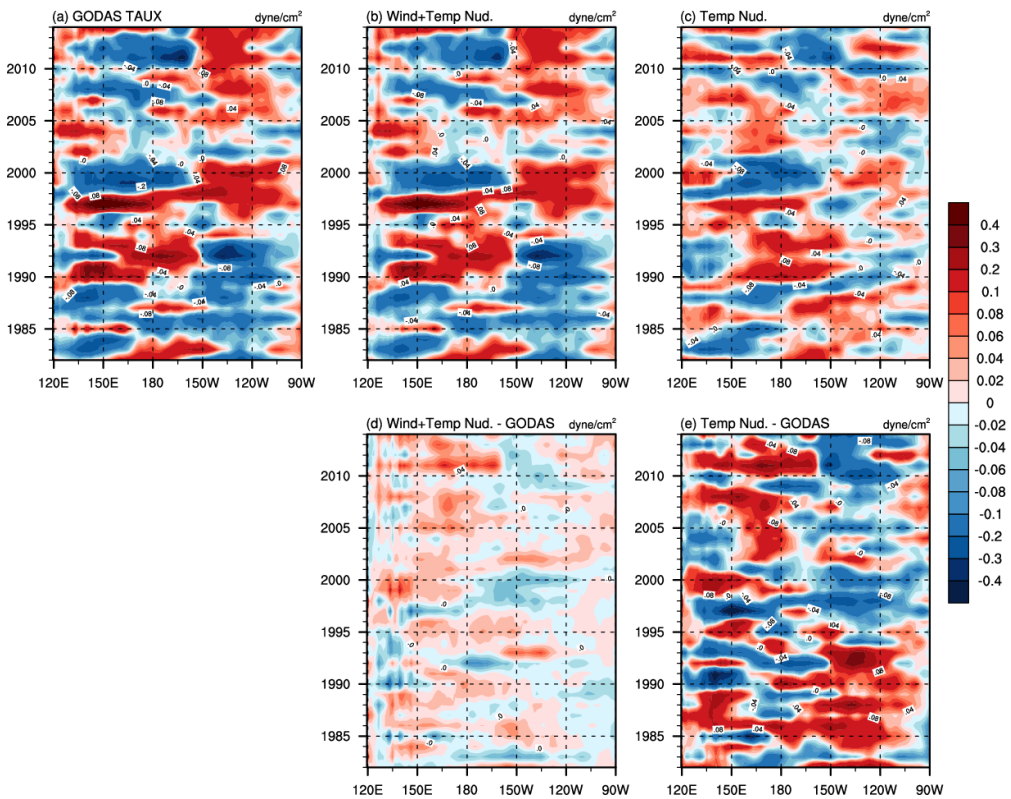

Figure 22 Wind stress (dyne cm^{-2}) anomalies along the equator from (a) the GODAS reanalysis data and the initial conditions generated with (b) the GODAS-WIND nudging and (c) the GODAS nudging method; and differences between the wind anomalies from (d) the GODAS-WIND nudging method and (e) the GODAS nudging method and those from the GODAS reanalysis data.

Therefore, it seems to be difficult to mimic all observed surface winds with the GODAS nudging method, since there are winds generated by the atmospheric circulation conditions as mentioned before. Considering the important role of the surface winds in the ENSO dynamics, we may expect improved prediction of the ENSO events. The results are shown in Figures 23 and 24.

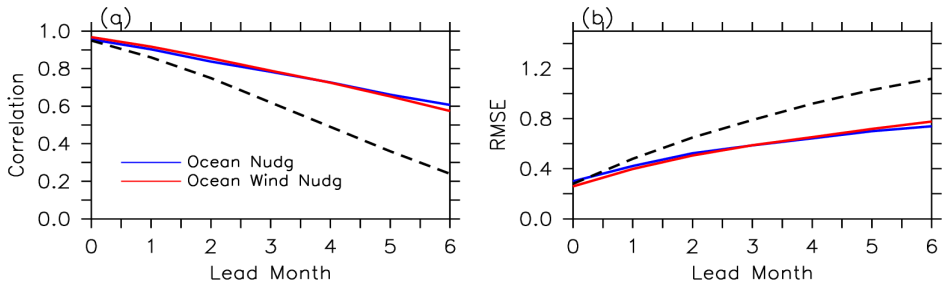

Figure 23 (a) TCC and (b) RMSE between the observed and predicted Niño 3.4 indices from 0- to 6-month lead times.

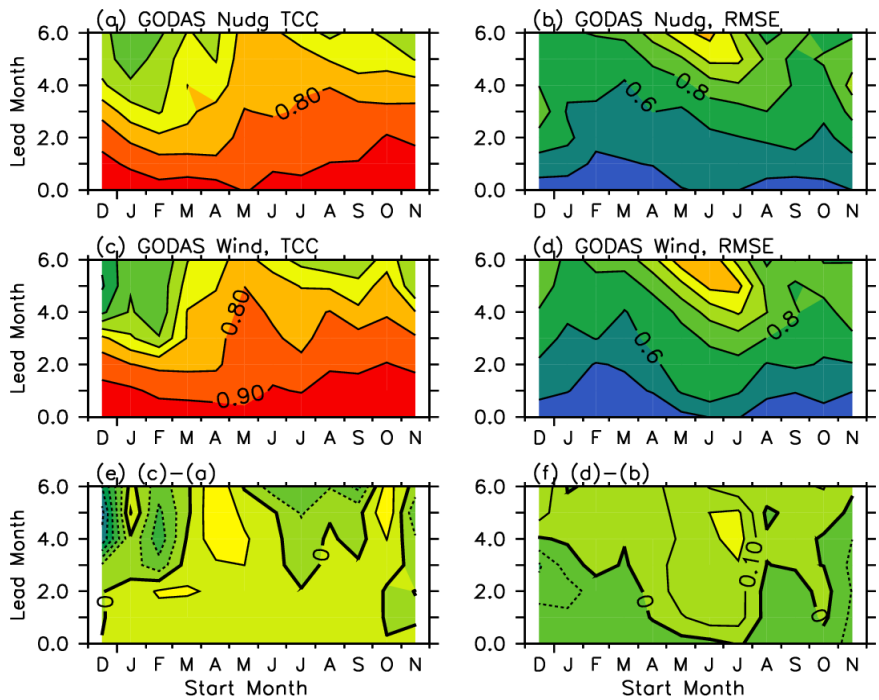

Figure 24 Seasonal stratification of the TCCs (left panels) and RMSEs (right panels) of the Niño 3.4 index predicted using (a, b) the GODAS nudging method and (c, d) the GODAS-WIND nudging method with respect to the observations; and differences in (e) TCC (C.I. = 0.05) and (f) RMSE (C.I.= 0.1 °C) between both methods.

Figure 23, which shows the TCCs and RMSEs of Niño 3.4 indices predicted with the GODAS nudging and the GODAS-WIND nudging methods with respect to the observations, illustrates that the application of the wind nudging to the initialization does not much affect the prediction skill of the overall ENSO, although there is slight improvement at early lead-month times. Some discernable difference is found when the prediction skill is evaluated by calendar month as shown in Figure 24. In this figure, we can recognize a slight increase in the TCCs through the 2-month lead times in the ENSO predictions with the GODAS-WIND nudging method relative to those with the GODAS nudging method, while there is a decrease in the TCC for winter (DJF) forecasts and summer (JAS) forecasts after a 3-month lead time. When the prediction of the Niño 3.4 index is performed using the spring (MAM) initial conditions, the GODAS-WIND nudging initialization method provides a better prediction skill, with a slower decrease in the TCC. This could be linked to the role of the WWBs in the ENSO onset season. Particularly, TCC values remain greater than 0.8 through the 5-month lead time period when using the initial conditions from May for the GODAS-WIND nudging method. As for the RMSE, during overall early lead month times, the GODAS-WIND nudging method shows a slightly better performance except for the May-July forecasts, in which the RMSEs of the Niño 3.4 forecasts with the GODAS-WIND nudging method is only slightly larger (>0.1°C) than those with the GODAS nudging initialization through all lead times.

To see if there is an improvement for strong El Niño forecasts starting in the spring season, we perform a composite analysis as displayed in Figure 25 for the time series of the composite Niño 3.4 index whose prediction is initialized in the end of April. For the composite analysis, we find 11 El Niño and 12 La Niña events in observations based on the methods from the Climate Prediction Center of the NOAA National Weather Service in the US where El Niño (La Niña) events are defined when the three-month running mean of the Niño 3.4 index continues to be greater than + 0.5 °C (-0.5 °C) for at least five over-lapping seasons. Then, using the DJF Niño 3.4 index, we classify strong, moderate, and weak El Niño events. When the DJF Niño 3.4 index is greater than 2.0°C, we define it as a strong El Niño. When the DJF Niño 3.4 index is between 1.0 and 2.0, we define it as a moderate El Niño. In a similar way, we also classify the La Niña events. The classification of the El Niño and La Niña events are shown in Table 1.

Table 1 Strong, moderate, weak El Niño and La Niña events over the period 1982-2014.

	Strong	Moderate	Weak
El Niño	1982/83, 1997/98	1986/87, 1991/92, 1994/95, 2002/03, 2009/10	1987/88, 2004/05, 2006/07, 2014/15
La Niña		1984/85, 1988/89, 1998/99, 1999/00, 2007/08, 2010/11	1983/84, 1995/96, 2000/01, 2005/06

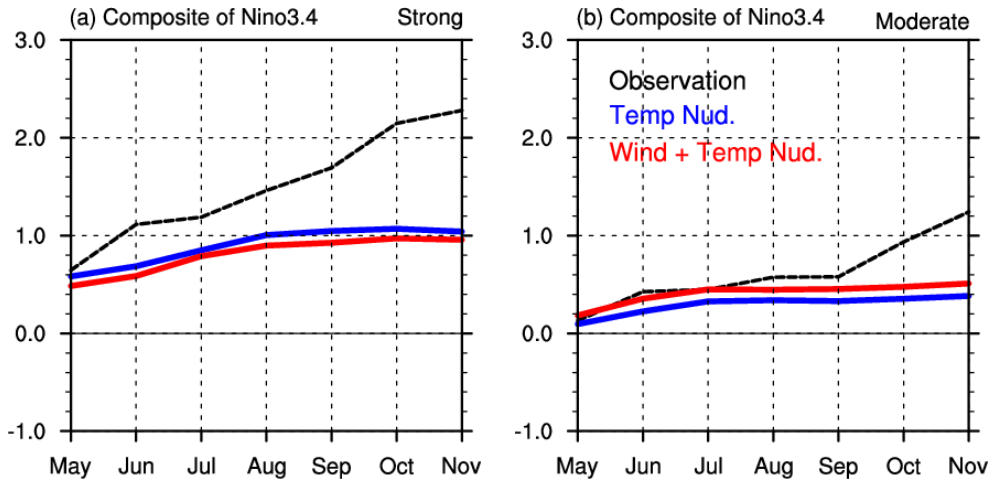

Figure 25 Time evolution of the composite Niño 3.4 index during the development (from May to November) of (a) strong and (b) moderate El Niño events from observations (black line) and predictions initialized in the end of April with the GODAS nudging (blue) and GODAS-WIND nudging (red) methods. Please see the main text for detail on the El Niño event years.

In Figure 25a, we find that forecasts of strong El Niño events are not successful with either initialization method. When the GODAS-WIND nudging method is used, we expect that WWBs, which are possibly retained in the initial conditions, could trigger and develop strong air-sea interactions by exciting downwelling Kelvin waves and, hence might be helpful for predicting observed strong El Niño events. It seems that the model discrepancies in simulating the ENSO as discussed in previous sections cannot be overcome just by adding a wind factor in the initial conditions when we try to provide good forecasts for strong El Niño events. Other factors such as model drift and its associated errors in the ENSO feedbacks may prevent the CCSM3 model from predicting the strong El Niño events, which will be discussed in next sections.

For the moderate El Niño cases (Fig. 25b), there is slight improvement when considering initial wind conditions. Until the third month after the April initialization with the GODAS-WIND nudging method, there are better predictions of El Niño strength.

4.3 Year-to-Year Variation of Forecast Skill

Figure 26 shows the ACC between the predictions at 1-and 3-month lead times initialized with the GODAS nudging method and observations over 33 winter seasons (DJF average). These are calculated over the tropical Pacific (120°E-90°W, 10°S-10°N) and the globe (0-360°E, 60°S-80°N). In this figure, to examine the relationship between the seasonal forecasting ability and the ENSO amplitude, we also superimpose the observed DJF averaged Niño 3.4 index (gray bar) with strong, moderate, and weak events indicated by a colored circle, a square, and a triangle, respectively (also see Table 1). From this figure, we can identify the year-to-year variation of the prediction skill of the tropical Pacific SST (Fig. 26a) and the global SST (Fig. 26b). The year-to-year change in the SST seasonal prediction skill is found to be strongly dependent on the intensity of the eastern tropical Pacific SST anomalies, which is consistent with previous studies (e.g., Kim et al., 2012). The ACC scores for the tropical Pacific SST are increased with the ENSO intensity, as is indicated in Figure 26c. For strong El Niño events (there is no strong La Niña event), the ACC average over two events is 0.92 at a 1-month lead time. Even for the 3-month lead time forecast of the tropical Pacific SST, the ACC is still strong at 0.83. For moderate ENSO events, the average of the ACC over the 11 events (five El Niño and six La Niña events) is greater than 0.7 for both lead time forecasts. During weak ENSO events, the tropical Pacific seasonal SST prediction skill is still acceptable with an ACC of 0.65 at a 1-month lead time. However, the ACC decreases quickly to 0.42 at a 3-month lead time. When the eastern equatorial Pacific SST anomalies are in a normal state, the CCSM3 model cannot provide skillful seasonal forecasts (ACC=0.39) as compared to the predictions for the strong and moderate events. For the global SST seasonal forecasts (Fig. 26d), we can reach a similar conclusion about the ENSO dependence on its prediction skill, even though the ACCs are smaller. It is during only strong and moderate El Niño events that the CCSM3 model can provide good predictions

(ACC=0.66 and 0.50, respectively) of the global SST anomalies at a 1-month lead time. These results are consistent with those from predictions using the GODAS-WIND nudging method (Fig. 27), which also shows the strong dependence of the tropical Pacific and global SST forecasts on the ENSO amplitudes.

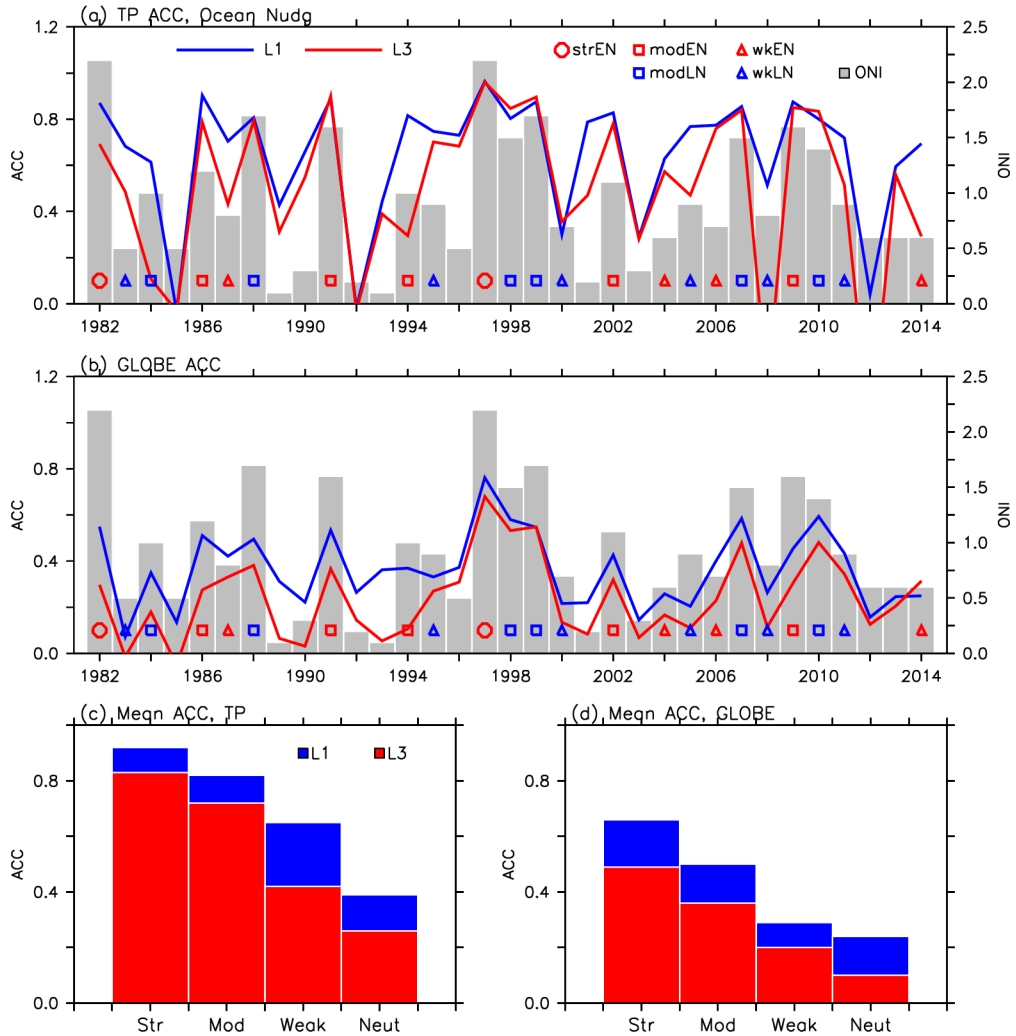

Figure 26 Time series of ACC of the DJF averaged SST anomalies in (a) the tropical Pacific (120°E-90°W, 10°S-10°N) and (b) the globe (0°-360E°, 60°S-80°N) predicted at 1-month (blue line) and 3-month (red line) lead times using the GODAS nudging initialization method; and average of the ACCs for the (c) tropical Pacific and (d) global SST over strong (Str), moderate (Mod), weak ENSO years and neutral (Neut) years at 1-month (blue bar) and 3-month (red bar) lead times. In (a) and (b), box plots for the absolute values (gray bars) of the observed DJF Niño 3.4 indices are superimposed and strong (circle), moderate (square), weak (triangle) El Niño (red) and La Niña (blue) events are indicated with a colored symbol.

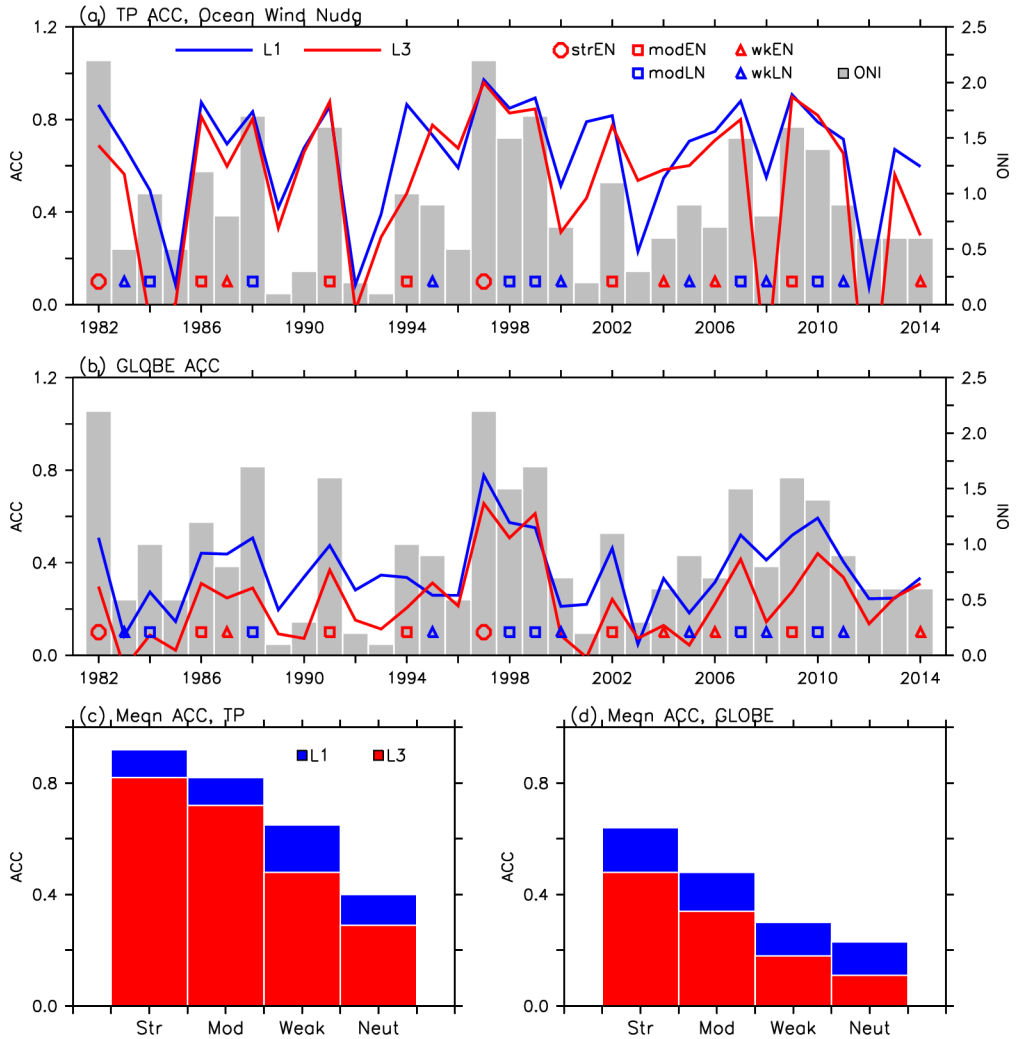

Figure 27 Time series of ACC of the DJF averaged SST anomalies in (a) the tropical Pacific (120°E-90°W, 10°S-10°N) and (b) the globe (0°-360E°, 60°S-80°N) predicted at 1-month (blue line) and 3-month (red line) lead times using the GODAS-WIND nudging initialization method; and average of the ACCs for the (c) tropical Pacific and (d) global SST over strong (Str), moderate (Mod), weak ENSO years and neutral (Neut) years at 1-month (blue bar) and 3-month (red bar) lead times. In (a) and (b), box plots for the absolute values (gray bars) of the observed DJF Niño 3.4 indices are superimposed and strong (circle), moderate (square), weak (triangle) El Niño (red) and La Niña (blue) events are indicated with a colored symbol.

4.4 ENSO Feedbacks and Model Drift

The model drift that climate state during the progress of forecast simulations tends to go toward the model climatology is inevitable. This drift may affect forecast errors in the intensity of an ENSO event. In Figure 28a, which shows a change in the ENSO amplitude with forecast lead times, the ENSO strength gradually decreases from the observed levels for both initialization methods. We can investigate which ENSO dynamics are related with the forecast error of the ENSO amplitude using

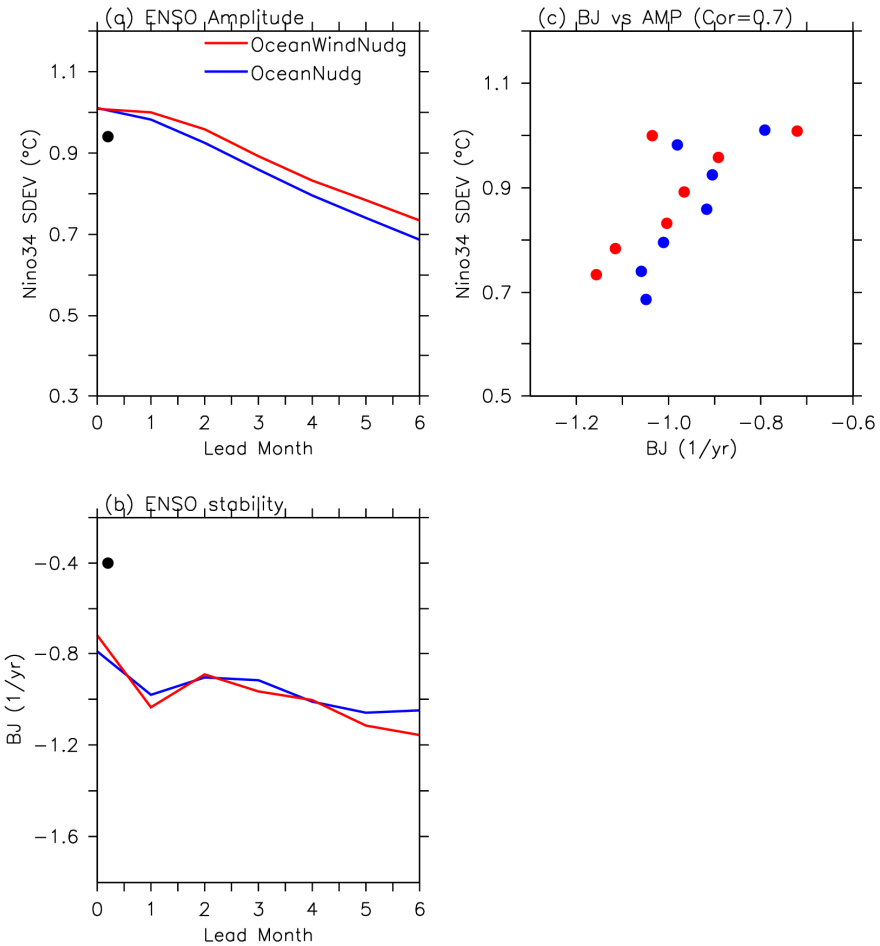

Figure 28 (a) ENSO amplitude (°C) with lead month time, (b) ENSO stability (yr^{-1}) as estimated with the BJ index, and (c) scatter plots of ENSO amplitude versus BJ index at 0-to 6-month lead times. Blue line and blue dots are for the GODAS nudging method and red line and red dots are for the GODAS-WIND nudging method. In (a) and (b), black dots indicate the observed ENSO amplitude and growth rate, respectively.

the BJ index analysis. Figure 28b displays that the growth rates, as estimated with the BJ index, tend to decrease with an increase in forecast lead time. Growth rates have a significant correlation with the ENSO amplitude (r=0.7), as shown in scatterplots of Niño 3.4 standard deviation versus BJ index (Fig. 26c). This result indicates that the BJ index analysis can provide insight into the forecasting errors of the ENSO amplitude based on ENSO dynamics.

Figure 29 shows the change in the feedback terms contributing to the BJ index with lead month times. Among positive feedback terms, the thermocline feedback term from the forecasts has a magnitude (about 0.6 yr^{-1}) comparable to that from the observations at early forecast lead months (e.g., 0-and 1-month lead times), but eventually the term decreases to 0.2 yr^{-1} at a 6-month lead time. On the other hand, other feedback terms do not show clear decreases with forecast lead times. Therefore, we may link the forecast error in the ENSO amplitude to that in the thermocline feedback. Taking a look at the mean state and the response sensitivity coefficients associated with the thermocline feedback term in Figure 30, we can find that the intensity of the zonal anomalous thermocline slope response to the winds (β_h) and the surface wind response to the SST change (μ_a) decreases as forecast lead time increases. Therefore, the errors of the thermocline feedback term can be related to those of the response sensitivity coefficients, which is consistent with previous numerical and observational studies showing that the change in the thermocline feedback is mainly controlled by changes in the zonal thermocline slope response to wind change (Kim et al., 2014; Lubbecke and McPhaden, 2013). Furthermore, their errors in coupled models are known to be attributable to the upper ocean cold bias in the tropical Pacific (Kim et al., 2014).

Therefore, we can examine the vertical cross section of the climatological ocean temperatures along the equator from predictions at 1-, 3-, and 6-month lead times and compare them to the GODAS reanalysis data as shown in Figure 31. It is found that the upper ocean cold bias tends to become stronger, particularly around the thermocline, which corresponds to an increase in the thermocline diffusion with lead times. As speculated by Kim et al. (2014), the diffusive thermocline may affect the intensity of the thermocline slope response to wind forcing. However, a more substantial analysis that evaluates subsurface ocean dynamics should be performed

to reveal which mechanisms are related to a change in the intensity of the thermocline slope response to wind forcing.

In conclusion, the mean drift or mean state bias in the coupled model can affect the prediction error of the ENSO amplitude, and we should endeavor to reduce various tropical Pacific climate biases in coupled models to provide better forecasts for the intensity of the ENSO events.

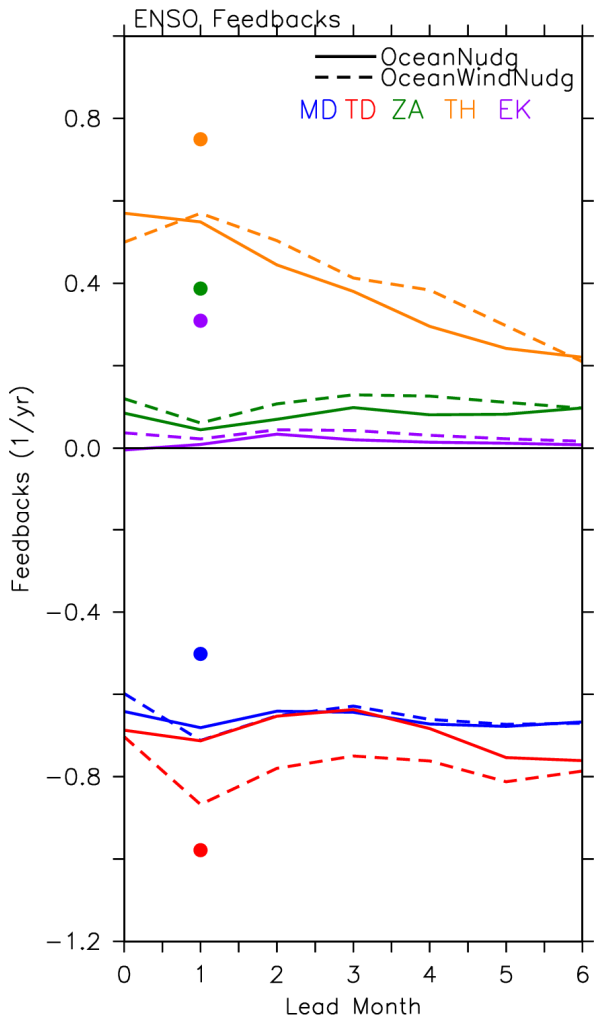

Figure 29 Feedback terms in the BJ index from predictions using the GODAS nudging (solid line) and the GODAS-WIND nudging (dashed lines) methods, which are calculated at each lead month time. Blue stands for mean advection damping, red for thermodynamic damping, green for zonal advective feedback, orange for thermocline feedback, and purple for Ekman feedback. Colored dots indicate results from the observations.

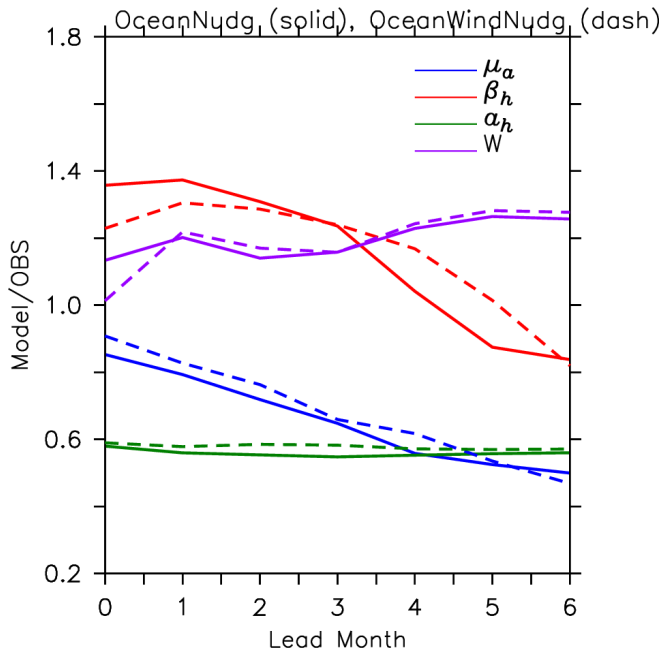

Figure 30 Change in mean state and response sensitivity coefficients associated with the thermocline feedback term as the forecast lead time increases from predictions with the GODAS nudging (solid line) and GODAS-WIND nudging (dashed lines) methods: wind response to the SST change (blue lines; μ_a), equatorial zonal thermocline slope response to wind change (red lines, β_h), the effect of ocean subsurface temperature on the SST (green lines, a_h), and mean upwelling (purple lines, W). They all are normalized by magnitudes from the observations.

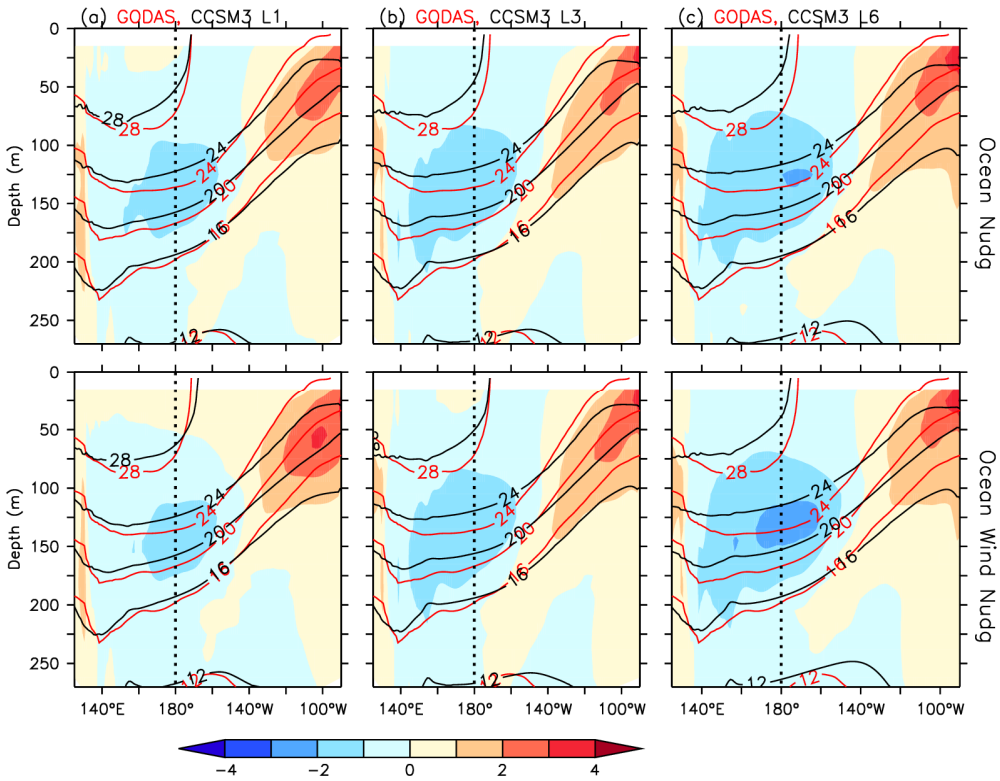

Figure 31 Climatology of subsurface ocean temperatures (°C; C.I. = 4°C) along the equator (2°S-2°N) from the GODAS reanalysis data (red contour lines) and from GODAS nudging (upper panels) and GODAS-WIND nudging methods (lower panels) (black contour lines) at (a) 1-month, (b) 3-month, and (c) 6-month lead times; and difference between the reanalysis data and the predictions (shades).

5. SUMMARY AND CONCLUDING REMARKS

In this project, we examined the systematic biases of the APCC-operating coupled models, CCSM3 and SCoPS, in simulating the observed tropical Pacific climate and the ENSO. The APCC coupled models can capture the key observed features of the tropical Pacific climate and the ENSO, but both models have several biases in common, including 1) an equatorial cold tongue that is too strong and extends too far to the west and warm biases in the extratropical northeastern and southeastern Pacific Oceans; 2) a thermocline that is too diffuse and weaker stratification that become worse toward the eastern Pacific Ocean; 3) precipitation that is too strong in the SPCZ and the ITCZ regions; 4) an ENSO that is shifted to the west and extends too far westward; 5) weaker wind and thermocline responses to the ENSO; and 6) the underestimation of zonal advective and thermocline feedbacks and thermodynamic damping among the ENSO related feedbacks.

We found some improvements with the SCoPS model, which will replace the CCSM3 model for operational forecasts of the seasonal climate in the near future. For instance, the SCoPS model can more realistically simulate the observed asymmetric feature of the annual mean rainfall in the north-south direction, the annual cycle of the SST, and the zonal winds along the equator. Spatial patterns of the ENSO and its related wind response and the temporal evolution patterns (lag regression) of equatorial SST anomalies, the zonal wind anomalies, the anomalous zonal currents, and the oceanic heat content anomalies associated with the ENSO are better simulated by the SCoPS model. However, the response of the rainfall and wind anomalies to the ENSO SST change is shifted too far to the west in the SCoPS model, compared with both the CCSM3 model and the observations. This may be due to an overly warm western tropical Pacific that likely makes rainfall response too sensitive to the SST change and to the penetration of a cold tongue into the central Pacific that makes the response confined to the western Pacific in the SCoPS model.

This project also attempted to improve the initial conditions in the CCSM3 model for better ENSO forecasts. The GODAS nudging initialization method makes it possible for the CCSM3 model to give better predictions of the ENSO amplitudes, the global

SSTs, and the extratropical air temperatures, since the initialization shocks occurring in predictions using the GODAS method are reduced with the improved initialization method. The rapid decrease of the TCCs with lead month times in the Niño 3.4 index predictions, which start from winter and early spring initial conditions using the GODAS method, is improved when using the GODAS nudging method. Furthermore, the rapid increase of the RMSE shown in the GODAS method when the ENSO forecasts start from the winter and summer season is also improved with the GODAS nudging method. Currently, the APCC CCSM3 model is providing the operational seasonal forecasts using the improved initialization method, namely the GODAS nudging method and is contributing to better forecasts from the APCC MME forecast system.

For improving the prediction skill of strong ENSO events or the ENSO amplitude, we also considered initial wind conditions (i.e., GODAS-WIND nudging). However, it was difficult to find discernable improvements in the ENSO forecasting with the GODAS-WIND nudging initialization method except for forecasts that initialized in the late spring (April-May) season.

It was also found that the APCC CCSM3 model has a year-to-year variation in the forecasts for the tropical Pacific and the global SST, which is due strongly to changes in the ENSO intensity. That is, their forecast skill increases with the ENSO intensity. This result shows the importance of obtaining accurate ENSO amplitude forecasts in order to obtain the better global and tropical Pacific SST predictions. Using the BJ index analysis, we attempted to find possible reasons for the increased errors in predicting the ENSO strength with the APCC CCSM3 model once forecasts start. We concluded that the forecast error for the ENSO amplitude may be related to the upper ocean cold bias and its associated diffuse thermocline in the tropical Pacific, which strongly affects the intensity of the thermocline feedback.

In this project, we found systematic biases in the tropical Pacific climate simulated by the APCC coupled models, namely in the CCSM3 and SCoPS models. It turns out that the biases strongly affect a level of skill in predicting the ENSO with the APCC CCSM3 coupled model. Therefore, we will continue to try to reduce the various tropical Pacific climate biases in the coupled models in order to provide better forecasts for the intensity of the ENSO events and the change in its associated global climate variables.

REFERENCE

AchutaRao, K. M., and K. R. Sperber, 2002: Simulation of the El Niño Southern Oscillation: Results from the Coupled Model Intercomparison Project. *Climate Dynamics,* **19**, 191–209.

AchutaRao, K. M., and K. R. Sperber, 2006: ENSO Simulation in Coupled Ocean-Atmosphere Models: Are the Current Models Better? *Climate Dynamics*, **27**, 1-15.

Adler, R. F., and Coauthors, 2003: The Version-2 Global Precipitation Climatology Project (GPCP) Monthly Precipitation Analysis (1979–Present). *Journal of Hydrometeorology*, **4**, 1147-1167.

Alexander, M. A., I. Blade, M. Newman, J. R. Lanzante, and N.-C. Lau, 2002: The atmospheric bridge: the influence of ENSO teleconnection on air-sea interaction over the global oceans. *Journal of Climate*, **15**, 2205-2231.

An, S.-I., and B. Wang, 2000. Interdecadal change of the structure of the ENSO mode and its impact on the ENSO frequency. *J. Climate***13**, 2044–2055.

An, S.-I., and F.-F. Jin, 2001: Collective role of thermocline and zonal advective feedbacks in the ENSO mode. *Journal of Climate*, **14**, 3421-3432.

Battisti, D. S., and A. C. Hirst, 1989: Interannual variability in a tropical atmosphere-ocean model: influence of the basic state, ocean geometry and nonlinearity. *Journal of the Atmospheric Sciences*, 46, 1687-1712.

Behringer, D. W., M. Ji, and A. Leetmaa, 1998: An improved coupled model for ENSO prediction and implications for ocean initialization. Part I: The ocean data assimilation system. *Monthly Weather Review*, **126**, 1013-1021.

Bellenger, H., E. Guilyardi, J. Leloup, M. Lengaigne, and J. Vialard, 2013: ENSO representation in climate models: from CMIP3 to CMIP5. *Climate Dynamics*, **42**, 1999-2018.

Briegleb, B. P., C. M. Bitz, E. C. Hunke, W. H. Lipscomb, M. M. Holland, J. L. Schramm, and R. E. Moritz, 2004: Scientific description of the sea ice component in the Community Climate System Model, Version Three. Tech. Rep. NCAR/TN-463STR, National Center for Atmospheric Research, Boulder, CO,78 pp.

Cai, W., P. van Rensch, T. Cowan, and H. H. Hendon, 2011: Teleconnection Pathways of ENSO and the IOD and the Mechanisms for Impacts on Australian Rainfall. *Journal*

of Climate, **24,** 3910-3923.

Cai, W., and Coauthors, 2014: Increasing frequency of extreme El Niño events due to greenhouse warming. *Nature Climate Change*, **4,** 111-116.

Chen, D., S. E. Zebiak, and M. A. Cane, 1997: Initialization and predictability of a coupled ENSO forecast model. *Mon. Wea. Rev.*, **125**, 773–788.

Chen, D., and Coauthors, 2015: Strong influence of westerly wind bursts on El Niño diversity. *Nature Geoscience*, **8,** 339-345.

Carton, J. A., and B. S. Giese, 2008: A reanalysis of ocean climate using Simple Ocean Data Assimilation (SODA). *Mon. Wea. Rev.*, **136**, 2999-3017.

Choi, J., S.-I. An, B. Dewitte, W.-W. Hsieh, 2009: Interactive feedback between the tropical Pacific decadal oscillation and ENSO in a coupled general circulation model, *J. Climate*, **22**, 6597-6611.

Chu, P. S., 1988: Extratropical forcing and the burst of equatorial westerlies in the western Pacific: A synoptic study. *Journal of the Meteorological Society of Japan*, **66**, 549–564.

Collins, W. D., and Coauthors, 2004: Description of the NCAR Community Atmosphere Model (CAM3). Tech. Rep. NCAR/TN464+STR, National Center for Atmospheric Research, Boulder, CO, 226 pp.

Collins, W. D., and Coauthors, 2006: The Community Climate System Model Version 3 (CCSM3). *Journal of Climate*, **19,** 2122-2143.

Cronin, M. F., N. A. Bond, C. W. Fairall, and R. A. Weller, 2006: Surface cloud forcing in the east Pacific stratus deck/cold tongue/ITCZ complex. *Journal of Climate*, **19**, 392-409.

deSzoeke, S. P., and S.-P. Xie, 2008: The Tropical Eastern Pacific Seasonal Cycle: Assessment of Errors and Mechanisms in IPCC AR4 Coupled Ocean–Atmosphere General Circulation Models. *Journal of Climate*, **21,** 2573-2590.

Eisenman, I., L. Yu, and E. Tziperman, 2005: Westerly wind bursts: ENSO's tail rather than the dog? *Journal of Climate*, **18,** 5224-5237.

Fedorov, A. V., S. Hu, M. Lengaigne, and E. Guilyardi, 2014: The impact of westerly wind bursts and ocean initial state on the development, and diversity of El Niño events. Climate Dynamics, 44, 1381-1401.

Fedorov, A. V., and G. S. Philander, 2001: A Stability analysis of tropical ocean–atmosphere Interactions: bridging measurements and theory for El Niño. *Journal of Climate*,

14, 3086-3101.

Goswami, B. N., and J. Shukla, 1991: Predictability of a coupled ocean-atmosphere model. *Journal of Climate*, **4,** 3-22.

Guilyardi, E., 2005: El Niño–mean state–seasonal cycle interactions in a multi-model ensemble. *Climate Dynamics*, **26,** 329-348.

Hirota, N., Y. N. Takayabu, M. Watanabe, and M. Kimoto, 2011: Precipitation Reproducibility over Tropical Oceans and Its Relationship to the Double ITCZ Problem in CMIP3 and MIROC5 Climate Models. *Journal of Climate*, **24,** 4859-4873.

Hoerling, M. P., and A. Kumar, 2002: Atmospheric response patterns associated with tropical forcing. *Journal of Climate*, **15**, 2184-2203.

Horel, J. D., and J. M. Wallace, 1982: Planetary-scale atmospheric phenomena associated with the Southern Oscillation. *Monthly Weather Review*, **109,** 813-829.

Hu, Z.-Z., B. Huang, Y.-T. Hou, W. Wang, F. Yang, C. Stan, and E. K. Schneider, 2011: Sensitivity of tropical climate to low-level clouds in the NCEP climate forecast system. *Climate Dynamics*, **36,** 1795-1811.

Hudson, D., O. Alves, H. H. Hendon, and G. Wang, 2010: The impact of atmospheric initialisation on seasonal prediction of tropical Pacific SST. *Climate Dynamics*, **36,** 1155-1171.

Hunke, E. C., and W. H. Lipscomb, 2010: CICE: The Los Alamos Sea Ice Model Documentation and Software User's Manual Version 4.1. LA-CC-06-012, T-3 Fluid Dynamics Group, Los Alamos National Laboratory, Los Alamos N.M.

Hwang, Y. T., and D. M. Frierson, 2013: Link between the double-Intertropical Convergence Zone problem and cloud biases over the Southern Ocean. *Proceedings of the National Academy of Sciences of the United States of America*, **110,** 4935-4940.

Jeong, H., 2013: Impact of ocean initialization on two type El Niño predictability in APCC CCSM3. *APCC Research Report2013-1*, APEC Climate Center, Busan (Korean article with English abstract).

Ji, M., D. W. Behringer, and A. Leetmaa, 1998: An improved coupled model for ENSO prediction and implications for ocean initialization. Part II: The coupled model. *Monthly Weather Review*, **126,** 1022-1034.

Jin, E. K., and J. L. Kinter III, 2008: Characteristics of tropical Pacific SST predictability in coupled GCM forecasts using the NCEP CFS. *Climate Dynamics*, **32,** 675-691.

Jin, F.-F., L. Lin, A. Timmermann, and J. Zhao, 2007: Ensemble-mean dynamics of the ENSO recharge oscillator under state-dependent stochastic forcing. *Geophysical Research Letters*, **34**.

Jin, F.-F., and S.-I. An, 1999: Thermocline and zonal advective feedbacks within the equatorial ocean recharge oscillator model for ENSO. *Geophysical Research Letters*, **26**, 2689-2992.

Jin, F.-F., S. T. Kim, and L. Bejarano, 2006: A coupled-stability index for ENSO. *Geophysical Research Letters*, **33**, L23708.

Jin, F.-F., 1997: An equatorial ocean recharge paradigm for ENSO. Part I: Conceptual model. *Journal of the Atmospheric Sciences*, **54**, 811-829.

Kanamitsu, M., W. Ebisuzaki, J. Woollen, S.-K. Yang, J. J. Hnilo, M. Fiorino, and G. L. Potter, 2002: NCEP–DOE AMIP-II Reanalysis (R-2). *Bulletin of American Meteorological Society,* **83**, 1631–1643.

Kao, H.-Y., and J.-Y. Yu, 2009: Contrasting Eastern-Pacific and Central-Pacific Types of ENSO. *Journal of Climate*, **22**, 615-632.

Kim, H.-J., and J.-B. Ahn, 2015: Improvement in Prediction of the Arctic Oscillation with a Realistic Ocean Initial Condition in a CGCM. *Journal of Climate*, **28**, 8951-8967.

Kim, H.-M., P. J. Webster, and J. A. Curry, 2012: Seasonal prediction skill of ECMWF System 4 and NCEP CFSv2 retrospective forecast for the Northern Hemisphere Winter. *Climate Dynamics*, **39**, 2957-2973.

Kim, S. T., and F.-F. Jin, 2011a: An ENSO stability analysis. Part I: results from a hybrid coupled model. *Climate Dynamics*, **36**, 1593-1607.

Kim, S. T., and F.-F. Jin, 2011b: An ENSO stability analysis. Part II: results from the twentieth and twenty-first century simulations of the CMIP3 models. *Climate Dynamics*, **36**, 1609-1627.

Kim, S. T., W. Cai, F.-F. Jin, and J.-Y. Yu, 2014: ENSO stability in coupled climate models and its association with mean state. *Climate Dynamics*, **42**, 3313-3321.

Kleenlyside, N., M. Latif, M. Botzet, and J. Jungclaus, 2005: A coupled method for initializing El Niño Southern Oscillation forecasts using sea surface temperature. *Tellus A*, **57**, 340-356.

Klein, S. A., 1999: Remote sea surface temperature variations during ENSO: evidence for a tropical atmospheric bridge. *Journal of Climate*, **12**, 917-932.

Kumar, A., H. Wang, Y. Xue, and W. Wang, 2014: How Much of Monthly Subsurface

Temperature Variability in the Equatorial Pacific Can Be Recovered by the Specification of Sea Surface Temperatures? *Journal of Climate*, **27,** 1559-1577.

Latif, M., and Coauthors, 1998: A review of the predictability and prediction of ENSO. *J. Geophys. Res.,* **103,** 14,375–14,393.

Lengaigne, M., and Coauthors, 2004: Triggering of El Niño by westerly wind events in a coupled general circulation model. *Climate Dynamics*, **23,** 601-620.

Li, G., and S.-P. Xie, 2014: Tropical Biases in CMIP5 Multimodel Ensemble: The Excessive Equatorial Pacific Cold Tongue and Double ITCZ Problems*. *Journal of Climate*, **27,** 1765-1780.

Lian, T., D. Chen, Y. Tang, and Q. Wu, 2014: Effects of westerly wind bursts on El Niño: A new perspective. *Geophysical Research Letters*, **41,** 3522-3527.

Lin J.-L., 2007: The double-ITCZ problem in IPCC AR4 coupled GCMs: Ocean-atmosphere feedback analysis. *J. Climate*, **20,** 4497-4524.

Lorenc, A. C., and F. Rawlins, 2005: Why does 4D-Var beat 3D-Var? *Quarterly Journal of the Royal Meteorological Society*, **131,** 3247-3257.

Lübbecke, J. F., and M. J. McPhaden, 2013: A Comparative Stability Analysis of Atlantic and Pacific Niño Modes*. *Journal of Climate*, **26,** 5965-5980.

Luo, J.-J., S. Masson, S. Behera, S. Shingu, and T. Yamagata, 2005: Seasonal Climate Predictability in a Coupled OAGCM Using a Different Approach for Ensemble Forecasts. *Journal of Climate*, **18,** 4474-4497.

McBride, J. L., N. E. Davidson, K. Puri, and G. C. Tyrell, 1995: The flow during TOGA COARE as diagnosed by the BMRC Tropical Analysis and Prediction System. *Monthly Weather Review*, **123**, 717–736.

McPhaden, M. J., 1999: Genesis and Evolution of the 1997-98 El Niño. *Science*, **283,** 950-954.

McPhaden, M. J., S. E. Zebiak, and M. H. Glantz, 2006: ENSO as an integrating concept in earth science. Science, 314, 1740-1745.

Oleson and Coauthors, 2004: Technical description of the Community Land Model (CLM). Tech. Rep. NCAR/TN-461+STR, National Center for Atmospheric Research, Boulder, CO, 174 pp.

Philander, G. S., 1983: Anomalous El Niño of 1982-83. *Nature*, **305,** 16-16.

Picaut, J., F. Masia, and Y. du Penhoat, 1997: An advective-reflective conceptual model for the oscillatory nature of the ENSO. *Science*, **277**, 663-666,

Rodgers, K. B., P. Friederichs, and M. Latif, 2004: Tropical Pacific decadal variability and its relation to decadal modulations of ENSO, *Journal of Climate*, **17**, 3761–3774.

Roeckner, E., G. Buml, L. Bonaventura et al., 2003: The atmospheric general circulation model ECHAM5. PART I: Model description. MPI Report 349, Max Planck Institute for Meteorology, Hamburg, Germany, P. 127.

Rosati, A., K. Miyakoda, and R. Gudgel, 1997: The impact of ocean initial conditions on ENSO forecasting with a coupled model. *Monthly Weather Review*, **125,** 754-772.

Saha, S., and Coauthors, 2006: The NCEP Climate Forecast System. *Journal of Climate*, **19,** 3483-3517.

Smith, R. D., J. K. Dukowicz, and R. C. Malone, 1992: Parallel ocean general circulation modeling. *Physica D*, **60**, 38-61.

Smith, T. M., and R. W. Reynolds, 2003: Extended reconstruction of global sea surface temperatures based on COADS data (1854-1997). *J. Climate*, **16**, 1495-1510.

Sun, J., and J.-B. Ahn, 2015: Dynamical seasonal predictability of the Arctic Oscillation using a CGCM. *International Journal of Climatology*, **35,** 1342-1353.

Sun, F. and J.-Y. Yu, 2009: A 10-15year Modulation Cycle of ENSO Intensity. *J. Climate*, **22**, 1718-1735.

Uppala, S. M., and Coauthors, 2005: The ERA-40 re-analysis. *Quarterly Journal of the Royal Meteorological Society*, **131,** 2961-3012.

Valcke, S., V. Balaji, A. Craig, C. Deluca, R. Dunlap, R. Ford, R. Jacob, J. Larson, R. O'Kuinghttons, G. Riley, M. Vertenstein, 2012: Coupling technologies for Earth System Modelling. *Geoscientific Model Development*, **5**, 1589-1596.

Vecchi, G. A., and D. E. Harrison, 2000: Tropical Pacific sea surface temperature anomalies, El Niño, and equatorial westerly wind events. *Journal of Climate*, **13,** 1814-1830.

Vecchi, G. A., 2006: The termination of the 1997-98 El Niño. Part II: Mechanisms of atmospheric change. *Journal of Climate*, **19,** 2647-2664.

Wang, B., R. Wu, and X. Fu, 2000: Pacific–East Asian teleconnection: how does ENSO affect East Asian climate? *Journal of Climate*, **13,** 1517-1536.

Wang, C.-C., W.-L. Lee, Y.-L. Chen, and H.-H. Hsu, 2015: Processes Leading to Double Intertropical Convergence Zone Bias in CESM1/CAM5. *Journal of Climate*, **28,** 2900-2915.

Wang, C., and J. Picaut, 2004: Understanding ENSO physics, A review, In: Earth's Climate:

The Ocean-Atmosphere Interaction. C. Wang, S.-P. Xie, and J. A. Carton, Eds., AGU Geophysical Monograph Series, **147**, 21-48,

Wang, C., L. Zhang, S.-K. Lee, L. Wu, and C. R. Mechoso, 2014: A global perspective on CMIP5 climate model biases. *Nature Climate Change*, **4,** 201-205.

Webster, P. J., and S. Yang, 1992: Monsoon and ENS: Selectively interactive systems. *Quarterly Journal of the Royal Meteorological Society*, **118**, 877-926.

Wittenberg, A. T., A. Rosati, N.-C. Lau, and J. J. Ploshay, 2006: GFDL's CM2 global coupled climate models. Part III: Tropical Pacific climate and ENSO. *Journal of Climate*, **19,** 698-722.

Xue, Y., B. Huang, Z.-Z. Hu, A. Kumar, C. Wen, D. Behringer, and S. Nadiga, 2010: An assessment of oceanic variability in the NCEP climate forecast system reanalysis. *Climate Dynamics*, **37,** 2511-2539.

Yu, J. Y., and C. R. Mechoso, 1999: Links between Annual Variations of Peruvian Stratocumulus Clouds and of SST in the Eastern Equatorial Pacific. *Journal of Climate*, **12**, 3305–3318.

Yu, J.-Y., and S. T. Kim, 2011: Reversed Spatial Asymmetries between El Niño and La Niña and Their Linkage to Decadal ENSO Modulation in CMIP3 Models. *Journal of Climate*, **24,** 5423-5434.

Zhang, C., 1996: Atmospheric intraseasonal variability at the surface in the tropical western Pacific Ocean. *Journal of the Atmospheric Sciences*, **53**, 739–758.

Zhang, G. J., and H. Wang, 2006: Toward mitigating the double ITCZ problem in NCAR CCSM3.*Geophysical Research Letters*, **33**, L06709.

Research Report 2015–06

Assessment of predicting and simulating the tropical Pacific climate with APCC Coupled General Circulation Models

Seon Tae Kim

APEC Climate Center
12 Centum 7-ro, Haeundae-gu, Busan 48058, Republic of Korea
Tel: +82-51-745-3900 Fax: +82-51-745-3949

www.apcc21.org

ISBN 979-11-5698-107-7